



Research Paper

Nanostructured Fe₂O₃ dispersed on SiO₂ as catalyst for high temperature sulfuric acid decomposition—Structural and morphological modifications on catalytic use and relevance of Fe₂O₃–SiO₂ interactions



Ashish Nadar^{a,e}, Atindra Mohan Banerjee^{a,*}, M.R. Pai^{a,e}, Sher Singh Meena^b, R.V. Pai^c, R. Tewari^{d,e}, S.M. Yusuf^{b,e}, A.K. Tripathi^{a,e}, S.R. Bharadwaj^a

^a Chemistry Division, Bhabha Atomic Research Centre, Mumbai 400085, India

^b Solid State Physics Division, Bhabha Atomic Research Centre, Mumbai 400085, India

^c Fuel Chemistry Division, Bhabha Atomic Research Centre, Mumbai 400085, India

^d Materials Science Division, Bhabha Atomic Research Centre, Mumbai 400085, India

^e Homi Bhabha National Institute, Anushaktinagar, Mumbai 400094, India

ARTICLE INFO

Article history:

Received 13 February 2017

Received in revised form 18 April 2017

Accepted 17 May 2017

Available online 21 May 2017

Keywords:

Water splitting

Sulfuric acid decomposition

ε-Fe₂O₃

High temperature catalyst

Nanorod

ABSTRACT

Through our previous studies it was established that non-precious Fe₂O₃ based catalyst has the potential to replace Pt based catalyst for high temperature sulfuric acid decomposition, the energy conversion step in iodine–sulfur or hybrid–sulfur thermochemical cycles for water splitting (Banerjee *et al.* [11] and [25]). However, issues like agglomeration and grain growth during prolonged operation still remain to be fully resolved. With an aim to develop low cost, abundant transition metal oxide catalyst with high activity and stability, Fe₂O₃ nanoparticles immobilized on SiO₂ support is explored, anticipating that the Fe₂O₃–SiO₂ interactions may prevent self agglomeration of Fe₂O₃ nanoparticles. Several catalysts with varying Fe₂O₃ content ranging from 5 to 20 wt% were synthesized, characterized and their catalytic activity evaluated. Structural investigations by XRD and Mössbauer spectroscopy revealed that the 1000 °C calcined samples contained ε-Fe₂O₃ as the major phase in addition to minor α and γ-Fe₂O₃ phases. ε-Fe₂O₃ were found to be dispersed as nanorods with typical width of 5 nm from HRTEM images. Analysis of surface features by N₂–BET surface area, pore size distribution, pore volume and XPS indicated that the majority of Fe₂O₃ was encapsulated within the mesoporous structure of SiO₂ upto 15 wt%, beyond which Fe₂O₃ was deposited outside the porous network in an enhanced quantity. The surface area of Fe₂O₃ (15 wt%)/SiO₂ was found to be 99.6 m²/g. Presence of Fe–O–Si linkages was confirmed by XPS, and supported by successive TPR/TPO studies. The extent of reducibility measured via TPR increased with increasing loading and was found to be maximum for the 15 wt% dispersed samples. The catalytic activity was found to increase with an increase in loading of active Fe₂O₃ content upto a SO₂ yield of ~92% at 900 °C at a WHSV of 27 g acid g^{−1} h^{−1}, for 15 wt% and then decreased. Further evaluation of the 15 wt% sample revealed the durability (100 h) and practical applicability of the composition. The surface morphology, structure and composition underwent modifications during the 100 h operation in order to adapt to the reaction environment (high temperature, steam, oxides of sulfur) and the Fe₂O₃ (15 wt%)/SiO₂ catalyst exhibited iron sulfate formation and significant surface reorganization. The high catalytic activity can be ascribed to nanoparticulate nature of Fe₂O₃ and stability due to its anchored structure on SiO₂. These findings would inspire the design of active and stable catalyst for high temperature catalytic reactions.

© 2017 Elsevier B.V. All rights reserved.

1. Introduction

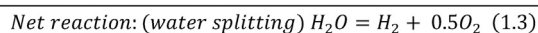
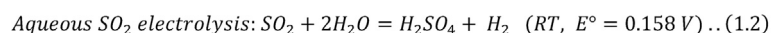
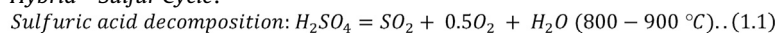
1.1. Thermochemical cycles for water splitting

“Thermochemical cycles for water splitting” utilize heat energy (thermo) to drive a set of chemical reactions (chemical) occur-

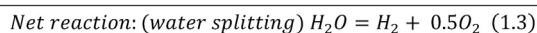
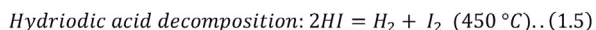
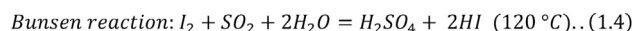
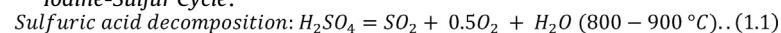
* Corresponding author at: Hydrogen Energy and Catalysis Section, Chemistry Division, Modular Labs, Bhabha Atomic Research Centre, Mumbai–400085, India.
E-mail addresses: atinmb@gmail.com, atinmb@barc.gov.in (A.M. Banerjee).

ring in a sequence (cycle), so that the net result is hydrogen and oxygen evolution from water (water splitting), alongside the recycling of all other chemicals involved. The thermal energy to drive the chemical reactions can be supplied by solar concentrators or high temperature nuclear reactors [1–5]. Depending upon the set of chemical reactions many thermochemical cycles for water splitting have been proposed in literature but among them iodine-sulfur or hybrid-sulfur thermochemical cycles hold promise by virtue of their higher efficiencies, feasibility of cyclic operation etc. [6]. Sulfuric acid decomposition is the highest temperature reaction in the iodine-sulfur or hybrid-sulfur (Westinghouse) thermochemical cycles (Eqs. (1.1)–(1.5)) [2,4]. In these cycles, sulfuric acid decomposition serves as the thermal energy storage step by extracting the solar/nuclear thermal energy, resulting in oxygen evolution and SO₂ generation from sulfuric acid (Eq. (1.1)). The generated SO₂ is utilized in other reactions of the cycles for hydrogen evolution and regeneration of sulfuric acid as shown in Eqs. (1.1)–(1.5).

Hybrid –Sulfur Cycle:



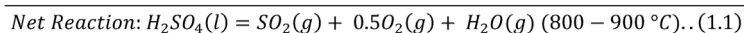
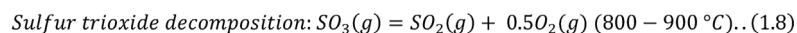
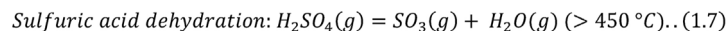
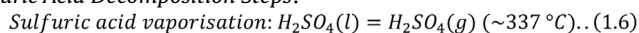
Iodine-Sulfur Cycle:



1.2. Sulfuric acid decomposition

Sulfuric acid decomposition reaction in the above thermochemical cycles progresses in several steps. The concentrated acid obtained from the relevant section of the cycles first vaporizes spontaneously above the boiling point of H₂SO₄ (337 °C, 1 atm., Eq. 1.6). The H₂SO₄ vapors dehydrate to produce SO₃ in the next step at reasonable rates (Eq. 1.7). But, the rate limiting reaction is the kinetically slow decomposition of the SO₃ molecule (Eq. 1.8) as this does not achieve thermodynamic conversions until a very high temperature is reached (>1100 °C) [7]. But, to enhance the efficiency of the above thermochemical cycles so that the process become economic, a catalyst is required to be employed to achieve the thermodynamic conversions at lower operating temperatures (750–900 °C) [7,8].

Sulfuric Acid Decomposition Steps:



1.3. Catalysts for sulfuric acid decomposition

Conventional Pt-based catalysts have been extensively employed in recent years, for the acid decomposition reaction, but the in-depth studies reveal that they suffer from several drawbacks viz. metal particle agglomeration, metal particle loss, metal oxidation, support sintering etc. [9,10] It was elucidated in our earlier investigation that Pt nanoparticles uniformly distributed over high surface area γ -Al₂O₃ suffered from Pt-agglomeration and a consequent reduction in Pt dispersion on 100 h use at 800 °C at a WHSV of 3.6 g acid g^{−1} catalyst h^{−1} [11]. In fact, finding a nanometer sized precious metal based active and stable catalyst for high temperature thermal reactions is a daunting job even today [12]. Thus, immense attention has been paid in search of suitable cheaper and stable alternatives to the Pt-catalyst for high

temperature catalytic reactions. In this regard transition metal oxide catalysts are promising candidates for a wide variety of chemical transformations by virtue of their low cost, possibility of synthesis in high surface area form, thermal stability, superior redox properties etc. The notable feature is the capability to tailor the catalytic properties of these oxides according to the targeted application by accommodating, substituting or doping various elements, a fact recently reviewed in several articles [13,14]. In line with these developments, researchers have investigated the functioning of oxide based catalysts for sulfuric acid decomposition to establish their suitability viz. Fe₂O₃-Al₂O₃, Fe₂O₃-TiO₂ [15]; complex oxides [16]; Fe/Cu/Al₂O₃ [17]; Fe₂O₃ based [18–20]; Copper pyrovanadate (Cu₂V₂O₇) [8]; Cu-V/SiO₂ [21]; copper hexa-oxo-divanadate (CuV₂O₆) [22]; as cheaper substitutes for Pt-based catalyst. In our earlier studies we established that Fe₂O₃ based catalysts can be a better and stable alternative to supported Pt catalyst for the high temperature sulfuric acid decomposition

[11,23–25]. However, issues like agglomeration during prolonged use at elevated temperatures need to be fully resolved. Also, it is imperative to attempt further improvements in the catalytic performance of iron oxide by exploring nanometer (1–10 nm) sized particles, as the catalytic properties in nanoscale is expected to be significantly boosted due to enhanced surface-to-volume ratio. But, the prolonged use of bare nanoparticles of Fe₂O₃ at high temperatures is bound to increase sintering rates resulting in faster grain growth. Even, for bulk Fe₂O₃ we observed severe particle agglomeration and sintering at high temperature prolonged use. An average particle size of ~100 nm in the fresh catalyst increased to ~200–400 nm after 100 h use at 800 °C [25]. To counter this, we had earlier exploited Cr-doping, [45], a strategy used in water gas shift reaction [25,26] where sintering is minimized by doping specific amounts of Cr in the active phase bulk Fe₃O₄. However, the average particle size of ~100 nm increased to ~150–300 nm

even in the case of Cr doped sample for sulfuric acid decomposition during 100 h operation under similar conditions [25].

In this work we have explored the effectiveness of Fe₂O₃/SiO₂ catalysts for high temperature sulfuric acid decomposition reaction, with emphasis on preparing Fe₂O₃ nanoparticles, determining the optimum content of Fe₂O₃ and elucidating their catalytic properties and stability during prolonged catalytic use. A twofold advantage is envisaged – first, it is expected to stabilize the nanometer sized Fe₂O₃ particles over the SiO₂ support to attain high catalytic activity and secondly, the active phase-support interaction (Fe₂O₃-SiO₂) is anticipated to decrease the active phase- active phase (Fe₂O₃-Fe₂O₃) interaction leading to reduced agglomeration rates at high temperatures and hence yield thermally stable compositions. The immobilization of nano particles of Fe₂O₃ has been carried out by adsorption and hydrolysis of iron-

acetylacetonate over amorphous SiO_2 . Detailed characterizations of the compositions were carried out using various techniques to probe the interactions between immobilized Fe_2O_3 and the support SiO_2 . The catalytic activities of all the materials were evaluated as a function of temperature from 700 °C to 900 °C. This temperature dependent activity would furnish an estimate of conversion at each temperature and correspondingly a measure of the highest operational temperatures for the solar thermochemical cycles [8,21]. The temperature of operation is critical with respect to material issues and efficiencies [2,4]. Subsequently the best composition was evaluated further for prolonged duration (100 h) to test its stability and also as a function of granular size, to ascertain the extent of catalyst diffusion limitations. The spent catalyst characterization was carried out to recognize the structural, morphological and thermal transformations occurring on the $\text{Fe}_2\text{O}_3/\text{SiO}_2$ system on the catalytic use for long duration. These studies will throw light on the effectiveness and durability of such catalytic systems for high temperature reactions.

2. Experimental

2.1. Preparation of $\text{Fe}_2\text{O}_3/\text{SiO}_2$ catalysts

2.1.1. Preparation of iron acetyl acetonate precursor

Fe(III) acetylacetonate, the precursor for Fe_2O_3 , was prepared by adding ferric chloride solution into an aqueous solution of sodium acetylacetonate in 1:3 molar ratio with continuous stirring. The red colored Fe (III) acetylacetonate precipitate was allowed to settle

overnight and then filtered through Buchner funnel. Solid obtained was dried in an air oven ($\sim 80^\circ\text{C}$) overnight. The purity of the sample was verified by melting point measurement.

2.1.2. Dispersion of Fe_2O_3 on SiO_2

The immobilization of Fe_2O_3 phase on SiO_2 (Evonik, Aeroperl 300/30) was carried out by an adsorption-equilibrium method or more appropriately by adsorption on SiO_2 and simultaneous hydrolysis of Fe(III) acetylacetonate as described schematically in Fig. 1 [27–29]. In brief, SiO_2 was well dispersed in 1-propanol by magnetic stirring and the pH of the solution was adjusted to 10 by adding NH_4OH . The temperature of this solution was maintained $\sim 0^\circ\text{C}$ by cooling with ice. A Fe(III) acetylacetonate solution was prepared with appropriate stoichiometry (so that the final product yields 5 wt% Fe_2O_3 in SiO_2) in a 1:1 water and 1-propanol mixture (solution A). Solution A was then added dropwise to the ice cooled solution of SiO_2 in NH_4OH . The mixed solution was aged overnight, filtered, the product washed several times with water and ethanol and dried in an air oven at 100°C overnight. This is the Fe_2O_3 (5 wt. %)/ SiO_2 as synthesized (FSO5as) product. The product was first calcined at 500°C for 4 h in air (FSO5-500) and then appropriately treated to either obtain the Fe_2O_3 (5 wt. %)/ SiO_2 (FSO5) catalyst or synthesize higher Fe_2O_3 content compositions as shown in Fig. 1.

To prepare the Fe_2O_3 (5 wt. %)/ SiO_2 sample, the 500°C calcined sample (FSO-500) was further heated at 1000°C for 5 h to get the final product (FSO5). To synthesize the Fe_2O_3 (10 wt. %)/ SiO_2 sample, the above method was repeated by replacing SiO_2 with the 500°C calcined Fe_2O_3 (5 wt. %)/ SiO_2 sample (FSO5-500) as shown in

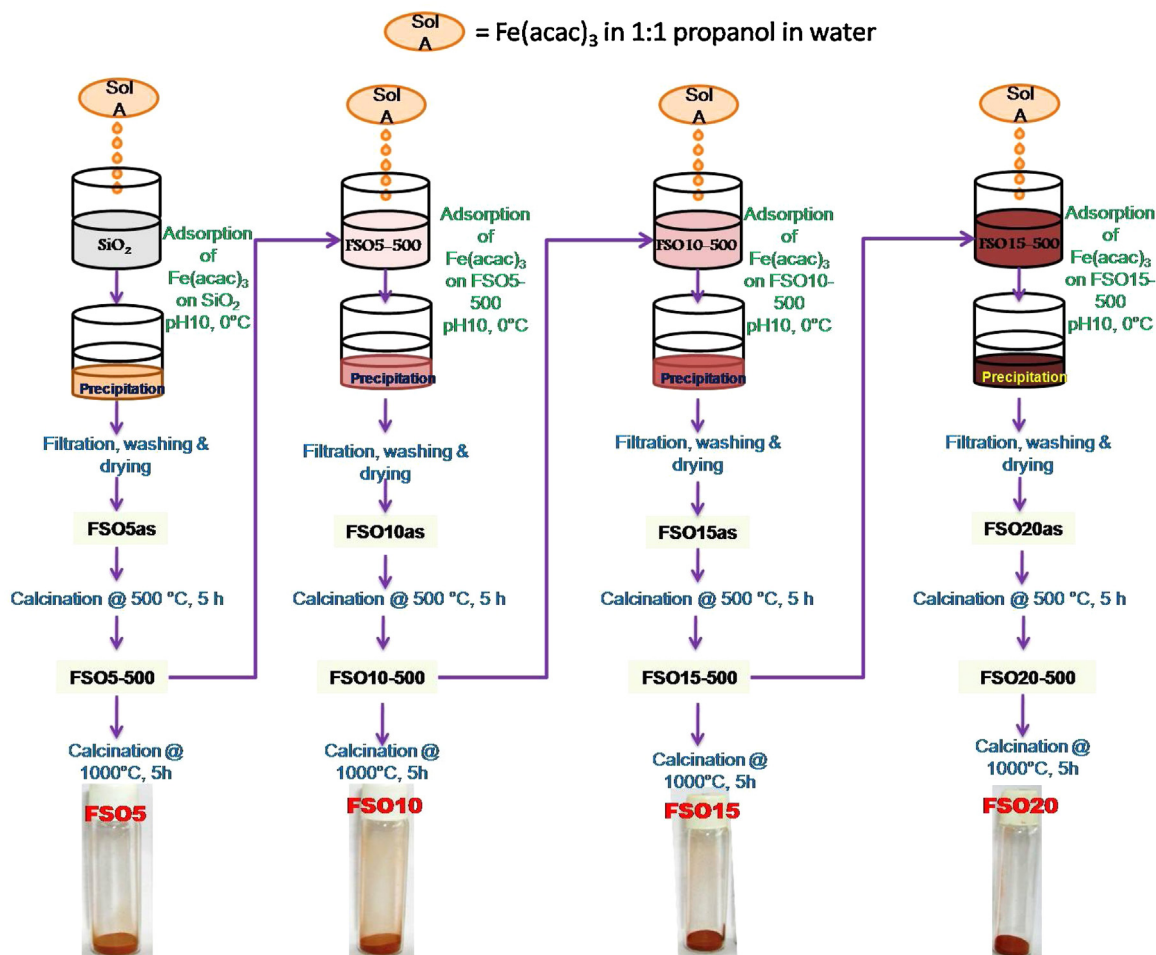


Fig. 1. Schematic representation of the preparation method of $\text{Fe}_2\text{O}_3/\text{SiO}_2$ catalyst with varying composition.

Fig. 1. Similarly to prepare the Fe_2O_3 (15 wt.%)/ SiO_2 sample, Fe_2O_3 (10 wt.%)/ SiO_2 was used instead of SiO_2 and so on. The final product in each case was calcined at 1000°C for 5 h to yield the functional catalyst. Heating rates for the calcination steps were maintained at 5°C min^{-1} . These catalysts, hereafter, are referred as FSOX, where, X represents the weight percent of iron oxide in the dispersed sample.

2.2. Fresh and spent catalyst characterization

The Fe_2O_3 content in each of the $\text{Fe}_2\text{O}_3/\text{SiO}_2$ catalysts was estimated using ICP-AES technique after microwave digestion of the powders in conc. HNO_3 – HCl (aqua regia). The powder XRD patterns were recorded on a Philips X'Pert pro X-ray diffractometer using $\text{Cu K}\alpha$ radiation ($\lambda = 1.5418 \text{ \AA}$) at 40 kV and 30 mA. Micromeritics ASAP-2020 surface area analyzer was employed for measurement of N_2 -BET surface area, pore size distribution and pore volume by recording the N_2 -adsorption-desorption isotherms. The pore size distribution and pore volume was determined from desorption isotherm using the BJH method. Room temperature Mössbauer spectra of all the samples were obtained using a spectrometer operating in constant acceleration mode in transmission geometry. The source employed was Co in Rh matrix of strength 50 mCi. The calibration of the velocity scale was carried out using iron metal foil. The outer line width of calibration spectrum was 0.29 mm/s. The Mössbauer data was analyzed using a least square fitting programme [24]. The redox properties of the samples as a function of temperature were determined by measuring the temperature programmed reduction/oxidation (TPR/O) using gas mixtures of 5% hydrogen in argon and 5% oxygen in helium for TPR and TPO respectively in TPDRO-1100 analyzer (Thermo Quest, Italy). The samples were pretreated at 350°C in helium for 3 h prior to each run. The morphological features were analyzed by recording the High resolution TEM (HR-TEM) images in a FEI-Tecna G-20 microscope operating at 200 kV. The X-ray photoelectron spectra were recorded on an electron spectrometer (SPECS, Surface Nano Analysis GmbH, Germany) using Mg–K α X-rays ($h\nu = 1253.6 \text{ eV}$) as the primary source of radiation with an overall energy resolution of about 0.7 eV. The appropriate corrections for charging effects were made with the help of a C 1 s signal appearing at 284.5 eV. The spent catalyst was also analyzed by XPS, SEM, HRTEM and Mössbauer spectroscopy to identify the morphological and structural changes arising out due to the 100 h catalytic operation in sulfuric acid decomposition reaction. To understand the nature of stable species produced on the catalyst during decomposition of sulfuric acid, the spent catalyst sample was heated in the temperature range of 400 – 1000°C at a heating rate of 10°C/min in a TG-DTA thermobalance and the evolved gases were analyzed by a QMS coupled to the TG-DTA, (SETSYS Evolution-1750, Setaram).

2.3. Catalytic activity measurements

The catalytic activities of all the dispersed samples were evaluated in a flow through quartz catalytic reactor (shown in Fig. S1, Supplementary Material). Concentrated sulfuric acid (98 wt.%) was loaded in a 50 ml syringe and injected into a quartz preheater at a flow rate of 0.05 ml min^{-1} held at 450°C . In the preheater liquid sulfuric acid is converted to sulfur trioxide and steam by vaporization and dehydration (as per Eqs 1.6–1.7). To carry this gas mixture into the catalyst zone N_2 gas was used as a carrier at a flow rate of 40 ml min^{-1} . In the catalyst zone sulfur trioxide decomposition occurs (as per Equation 1.8) to produce sulfur dioxide and oxygen. 200 mg of the catalyst was loaded in the catalyst zone and the temperature of the zone was maintained with a temperature controller. After exiting from the catalytic reactor, the products along with the unreacted reactants proceeds to the condenser where unreacted sulfuric acid is condensed and the sulfur dioxide is later trapped

in a sodium hydroxide solution and measured using chemical titrimetric methods. The catalytic activity was quantified by the extent of SO_2 yield defined as:

$$\text{Percentage } \text{SO}_2 \text{ Yield} = \frac{\text{No. of moles of } \text{SO}_2 \text{ produced}}{\text{No. of moles of } \text{H}_2\text{SO}_4 \text{ in feed}} \times 100$$

The catalytic activity of all the $\text{Fe}_2\text{O}_3/\text{SiO}_2$ catalysts (40–80 mesh; ASTM) was measured as a function of temperature between 700 and 900°C at a WHSV of $27 \text{ g acid g}^{-1} \text{ h}^{-1}$. Prior to each run the catalyst was degassed at a temperature of 500°C for 2 h at a N_2 flow rate of 40 ml min^{-1} . To achieve equilibrium the catalyst was held at each temperature for 30 mins and then measurement was initiated. Several measurements were made in $\sim 2 \text{ h}$ duration kept at each temperature. FSO15 exhibited highest temperature dependent catalytic activity as discussed in details later. Further, to get a quantitative measure of the diffusion limitation in the most active catalyst composition, the SO_2 yield was evaluated at 800°C with FSO15 catalyst for three different catalyst particle sizes 45–80 mesh, 20–45 mesh and 10–20 mesh. Finally, to determine the stability of the most active catalyst, a 100 h time on stream performance for sulfuric acid decomposition was evaluated for the FSO15 (20–45 mesh) and the catalyst was recovered and spent catalyst characterized.

3. Results and discussions

3.1. Efficacy of the method of preparation

The immobilization of Fe_2O_3 on SiO_2 was carried out by the adsorption equilibrium method as shown in Fig. 1 [27–29], which involved drop wise addition of Fe(III) acetylacetonate (Solution A) to an ice cooled alkaline solution (precipitant) of suspended SiO_2 . The chemical process involved the hydrolysis of the Fe(III) acetylacetonate (catalyst precursor) into Fe-hydroxide (the precipitate). The insoluble precipitate is immobilized (adsorbed) onto the support which is generated slowly in solution (equilibrium), and subsequently its concentration is raised homogeneously. Under vigorous agitation of the suspended SiO_2 solution, a rapid distribution of the precipitant-precursor is ensured and precipitation occurs homogeneously while hydrolysis of the bulky precursor at low temperature ensures slow generation of the precipitate. To analyze the complete hydrolysis of iron acetylacetonate and immobilization of iron oxide species, the thermo-gravimetric analysis of the Fe (III) acetylacetonate ($\text{Fe}(\text{acac})_3$), the as-synthesized 5 wt.% sample (FSO5as) and the 500°C calcined sample (FSO5-500) was recorded and the TG pattern is shown in Fig. S2 (Supplementary Material). The Fe(III) acetylacetonate undergoes thermal decomposition with onset of weight loss at $\sim 170^\circ\text{C}$. The decomposition products were analyzed by recording the FTIR spectra of the evolved gases *in-situ*. The evolution of CO_2 and acetone was observed at 305°C and 597°C respectively (Fig. S3, Supplementary Material) which is in agreement with reported literature [30]. The as-synthesized and the calcined 5 wt.% Fe_2O_3 samples did not undergo any appreciable thermal weight loss phenomenon and neither any gas was detected in the outlet by FTIR, confirming the completion of hydrolysis of iron acetylacetonate. To further confirm this aspect it was observed that the FTIR spectra of Fe(III) acetylacetonate showed characteristic peaks due to Tris(2,4-pentanedionato) Iron [31], while, no presence of acetyl acetate species were observed in the 500°C calcined sample (FSO5-500) or even in the as-synthesized 5 wt.% dispersed sample (FSOas) (Fig. S4, Supplementary Material). Moreover, in FSOas and FSO5-500 a shoulder appears due to the presence of Fe–O bond stretching in iron oxides [25]. This, not only confirms the complete hydrolysis of the Fe(III) acetylacetonate but also formation of iron-oxygen species in the

Table 1
Sample composition of Fe₂O₃ dispersed on SiO₂ with weight percentage (w/w) in parenthesis, sample abbreviation, N₂-BET surface area, pore size and pore volume of the samples.

Nominal Sample Composition	Sample Abbreviation (1000 °C calcined)	Actual Composition (ICPAES)	N ₂ -BET Surface Area	Pore Size	Pore Volume
Fe ₂ O ₃ wt.% on SiO ₂		Fe ₂ O ₃ wt.% on SiO ₂	(m ² /g)	nm	cm ³ /g
SiO ₂	SiO ₂		249.5	26.9	1.8
Fe ₂ O ₃ (5%)/SiO ₂	FSO5	4.6	147.6	28.5	1.3
Fe ₂ O ₃ (10%)/SiO ₂	FSO10	9.8	120.0	29.5	1.1
Fe ₂ O ₃ (15%)/SiO ₂	FSO15	14.0	99.6	31.8	0.9
Fe ₂ O ₃ (20%)/SiO ₂	FSO20	17.6	100.9	26.9	0.8

as-synthesized product. Thus, the effectiveness of this process for the preparation of dispersed Fe₂O₃ nano particles is established.

3.2. Determination of actual Fe₂O₃ content in the catalyst

The composition of the samples synthesized, their abbreviation and the actual amount of Fe₂O₃ (w/w) dispersed on SiO₂ catalysts as determined by elemental composition analysis using ICP-AES technique are listed in Table 1. It is evident from Table 1 that the samples synthesized contain almost the expected amount of Fe₂O₃, with the exception of the highest composition, where a lower amount of Fe₂O₃ is deposited than expected. A probable cause for such a phenomenon might be that an optimum concentration of Fe₂O₃ on SiO₂ might have reached and excess iron species was unable to get incorporated within the SiO₂ matrix.

3.3. N₂ adsorption-desorption isotherm

Table 1 also lists the N₂-BET surface area, pore size and pore volume of the samples. As can be seen from the Table, the BET surface area drops down drastically from 249.47 m²/g for bare SiO₂ to 147.61 m²/g as 5 wt.% Fe₂O₃ is deposited on it. This drastic decrease is mainly due to coupled effect of the calcination steps at 500 °C and 1000 °C and the deposition of Fe₂O₃ on SiO₂ surface, thus Fe₂O₃ blocking the surface sites of SiO₂. On further dispersion of the active component Fe₂O₃, on the SiO₂ substrate, a progressive decrease in surface area is observed. Only in the case for the extreme composition FSO20 the surface area does not undergoes any further decrease. The above result possibly signifies that the Fe₂O₃ is well deposited on the surface sites of SiO₂ and a maximum dispersion is probably reached at ~15 wt.%.

The N₂ adsorption desorption isotherm and the pore size distribution plots for these samples (shown in Fig. S5, Supplementary Material) exhibits Type-IV isotherm with hysteresis, typical of mesoporous character. It is thus evident that the mesoporosity is retained in all the samples. The pore volume also exhibits a similar trend as surface area and a progressive decrease in its value is observed with an increase in Fe₂O₃ content. Interesting feature is seen in the case of pore size of the samples. Bare SiO₂ exhibits a pore size of ~26.9 nm. The pore size increased gradually as Fe₂O₃ was deposited on the SiO₂ surface signifying incorporation of Fe₂O₃ moieties inside the pores and its consequent enlargement to accommodate the nanosized Fe₂O₃ particles. This trend continues till 15 wt.% dispersed samples where a maximum value of pore diameter of ~31.8 nm is observed. Thus maximum dispersion of Fe₂O₃ within the pores of SiO₂ took place for the 15 wt.% dispersed sample leading to maximum pore opening. The pore size for FSO20 reverted back to 26.9 nm, a suggestion of Fe₂O₃ agglomeration and enhanced precipitation outside the pore structure of the support. The result indicates that significant amount of Fe₂O₃ remains confined within the mesoporous network of SiO₂ matrix till FSO15. But beyond this composition, Fe₂O₃ mostly precipitates outside the pores of SiO₂ and also agglomerates of Fe₂O₃ blocked the pore openings, since the pore volume, on the contrary, decreased fur-

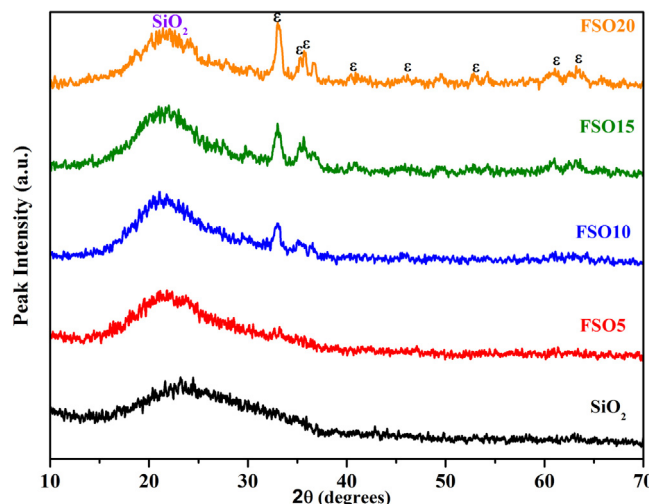


Fig. 2. Powder XRD patterns of the silica support and 1000 °C calcined Fe₂O₃/SiO₂ samples.

ther than FSO15. However, we can conclude from the above studies that the porous network of SiO₂ undergoes significant deformation on the Fe₂O₃ immobilization and the degree of distortion directly depends on the extent of Fe₂O₃ deposited.

3.4. Phase identification by powder XRD and Mössbauer spectroscopy

Fe₂O₃ is a well known polymorph existing in four different crystalline forms: α-Fe₂O₃ (mineral name: hematite, corundum structure, space group $R\bar{3}c(167)$), β-Fe₂O₃ (bixbyite structure, space group $Ia\bar{3}(206)$), γ-Fe₂O₃ (mineral name maghemite, spinel structure with disordered vacancies, space group $Fd\bar{3}m(227)$, or alternate structures), and ε-Fe₂O₃ (isostructural with κ-Al₂O₃, space group $Pna2_1(33)$) [32,33]. Determination of the Fe₂O₃ phase in a dispersed sample like ours is rather difficult due to its low content and nanocrystalline nature. In fact, structural studies related to phase transformations of Fe₂O₃ dispersed on SiO₂ as a function of temperature is a demanding topic in view of its vast application and separately investigated in recent times [32–35]. Phase identification in our Fe₂O₃/SiO₂ dispersed samples was first attempted by recording and analyzing the powder XRD patterns. The powder-XRD patterns of all the 1000 °C calcined samples are shown in Fig. 2. The support SiO₂ exhibits a broad hump centered at peak position 2θ ~22° (mineral name: cristobalite, tetragonal crystal system, Space Group: $P4_12_12(92)$, ICSD No. 47219). Peaks due to Fe₂O₃ were not clearly visible in FSO5 probably due to the low iron oxide phase content. In higher Fe₂O₃ containing samples broad peaks due to various phases appeared. In FSO10 peaks due to ε-Fe₂O₃ phase (orthorhombic crystal system, ICSD No. 415250) were present. In FSO15 and FSO20, minor peaks due to α- and γ-Fe₂O₃ were also visible. The 100% peak of ε-Fe₂O₃ (ICSD No. 415250); γ-Fe₂O₃ (ICSD

No. 172905) and α -Fe₂O₃ (ICSD No. 15840) appeared at peak positions $2\theta = 33.05, 35.6$ and 33.2° respectively. In all the above three samples the peak due to the ε -Fe₂O₃ phase was most prominent and intense signifying that this phase has the major contribution in the 1000 °C calcined samples.

The crystal structure of the three different polymorphs identified in our sample are shown in Fig. S6 (Supplementary Material). In our earlier study with bare Fe₂O₃ nanoparticles we obtained α -Fe₂O₃ as the lone crystalline phase upon calcination at 750 °C [25]. In this study, the intensity pattern of powder XRD suggests that this phase might be present in minor quantity. It is one of the most common and the most thermally stable polymorph of Fe₂O₃ and is generally produced by thermal decomposition of a wide variety of iron (II) and iron (III) compounds and also by thermal transformations of other iron oxide polymorphs [34,35]. From Fig. S6 (Supplementary Material) it is evident that it comprises of a hexagonal close packed array of oxide ions with ferric ions occupying two-thirds of the octahedral interstices giving rise to eight cations in the first neighbor sphere. Thus all the Fe sites are equivalent. Its rhombohedral unit cell contains six formula unit with lattice parameters of $a = 5.036 \text{ \AA}$ and $c = 13.749 \text{ \AA}$ [23,25,34–36]. The other common Fe₂O₃ phase is the γ -Fe₂O₃ or maghemite which is also present in minor amounts in the 1000 °C calcined samples. Generally, the lower temperature nanometer sized stable phase is the γ -Fe₂O₃ phase and it exhibits superparamagnetism in nanoparticle form [35,36,39]. It exhibits a cubic crystal structure (Fig. S6) ($a = 8.351 \text{ \AA}$) of an inverse spinel type with cationic vacancies either randomly distributed (space group $Fd\bar{3}m$) or an ordered vacancy structure (space group $P4_332$ and/or $P4_132$). Thus, Fe occupies two non-equivalent sites. In the current study we have obtained ε -Fe₂O₃ as the major phase. This Fe₂O₃ phase is orthorhombic and not as common as the above two with very rare natural occurrence and is generally obtained as an intermediate phase (with intermediate structural features) during the thermal transformation of cubic spinel γ -Fe₂O₃ nanostructured phase to a rhombohedral corundum α -Fe₂O₃ polymorph when dispersed over SiO₂ [32–35]. ε -Fe₂O₃ exhibits an orthorhombic crystal structure with a space group of $Pna2_1$ and lattice parameters $a = 5.072 \text{ \AA}$, $b = 8.736 \text{ \AA}$, $c = 9.418 \text{ \AA}$. The structure consists of three nonequivalent anion (A, B and C) and four cation (Fe1, Fe2, Fe3 and Fe4) positions. Fe4 is tetrahedrally coordinated, while Fe1, Fe2, Fe3 are octahedrally coordinated [36]. Anyways, controlled synthesis of ε -Fe₂O₃ alone is a tough task and is currently being studied by gaining control over the kinetics of γ -Fe₂O₃ to ε -Fe₂O₃ transformations [33,34].

⁵⁷Fe Mössbauer spectroscopy is a unique method to distinguish and identify different structural forms, amorphous or nanostructured Fe₂O₃ particles [24,36,37]. In order to determine the oxidation state of Fe, structure of the oxide and extent of nanocrystallinity, the room temperature Mössbauer spectra were recorded for FSO10, FSO15 and FSO20 and is shown in Fig. 3. The values of different Mössbauer parameters are given in Table 2. The room temperature Mössbauer spectra of samples calcined at 1000 °C can be fitted with four sextets (Zeeman splitting patterns) and a superparamagnetic doublet. The identification of different phases of iron oxide were done based on the values of isomer shift (δ), Quadrupole splitting (Δ) and Hyperfine field (H_{hf}). α -Fe₂O₃ exhibits only one sextet (sextet A) due to the octahedrally placed Fe at equivalent 12c crystal sites. It exhibits the following room temperature hyperfine parameters – isomer shift (δ) Fe (isomer shift related to metallic iron) ~ 0.329 – 0.396 mm/s , Quadrupole splitting (Δ) of ~ -0.22 – 0.28 mm/s , and Hyperfine field (H_{hf}) of $\sim 51 \text{ T}$. The other three sextets, B (Fe₁ and Fe₂), C (Fe₃) and D (Fe₄) belong to ε -Fe₂O₃ phase. Although ε -Fe₂O₃ consist of four non-equivalent Fe sites, two of the three octahedral sites overlap due to close values of Hyperfine field [36] and is difficult to distinguish in our spectra. The Hyperfine field values differentiates the octahedral sites (Fe1, Fe2 & Fe3, $H_{\text{hf}} \sim 45$ &

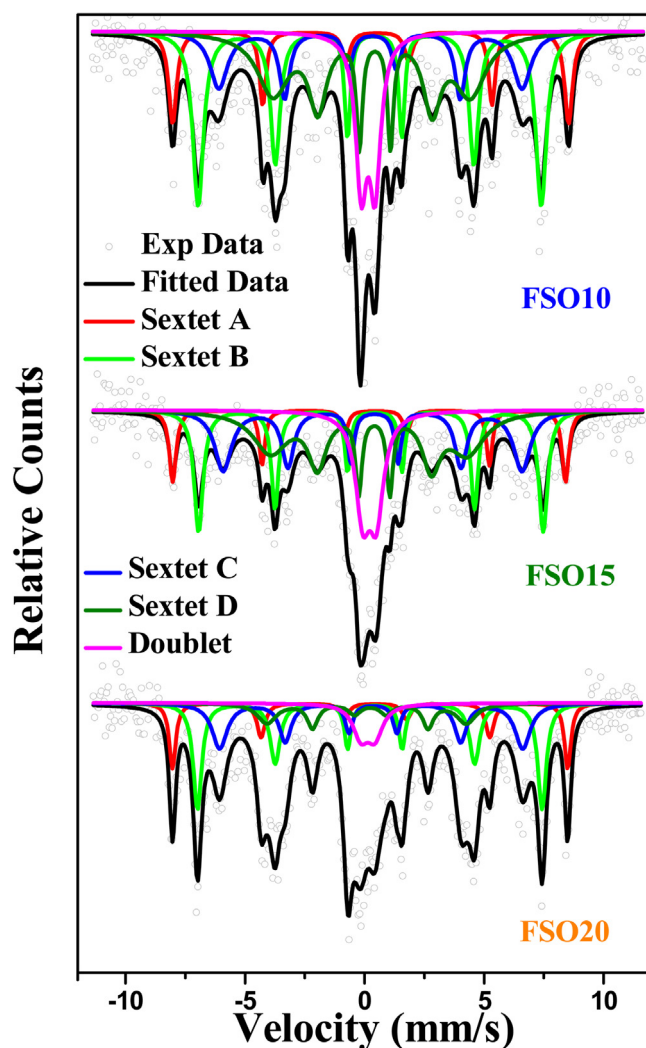


Fig. 3. Room Temperature Mössbauer spectra of the dispersed Fe₂O₃ samples calcined at 1000 °C for 5 h.

39 T) from the tetrahedral site (Fe4, $H_{\text{hf}} \sim 25 \text{ T}$). The doublet belongs to superparamagnetic γ -Fe₂O₃ phase [36–38]. Hence, the observed Mössbauer spectra are due to contribution of all three phases of iron oxide. The relative area of the three phases as calculated from the area under the curve was found to be: ε -Fe₂O₃ ($\sim 74.5\%$) > α -Fe₂O₃ (16.7%) > γ -Fe₂O₃ (8.8%) for FSO20 sample. Thus, in accordance with powder XRD results, the major phase in the samples is found to be in ε -Fe₂O₃ form.

It is pertinent to mention here that the room temperature Mössbauer spectra of all the dispersed samples calcined at 500 °C exhibited a single superparamagnetic doublet mostly due to the existence of γ -Fe₂O₃ nanoparticles dispersed over SiO₂ (Fig. S7, Supplementary Material). The single doublet represents γ -Fe₂O₃ nanoparticles in which long range magnetic ordering is absent. This clearly authenticates the fact that till 500 °C calcination, Fe₂O₃ dispersed on SiO₂ exist only in γ -phase. Further, the variation in isomer shift (δ), quadrupole splitting (Δ), line width (Γ) as a function of Fe₂O₃ content are shown in Fig. S5, ESI. Quadrupole splitting values increased with increasing Fe₂O₃ content, indicating an increase in distortion as shown in Fig. S5 and as found earlier the distortion do not further increase for the 20 wt.% dispersed samples. The line width (Γ) was found to lie between 0.662 – 0.699 mm s^{-1} for all compositions due to presence of particles in the nanometer range. Thus, the ε -Fe₂O₃ in our sample could be the stable intermedi-

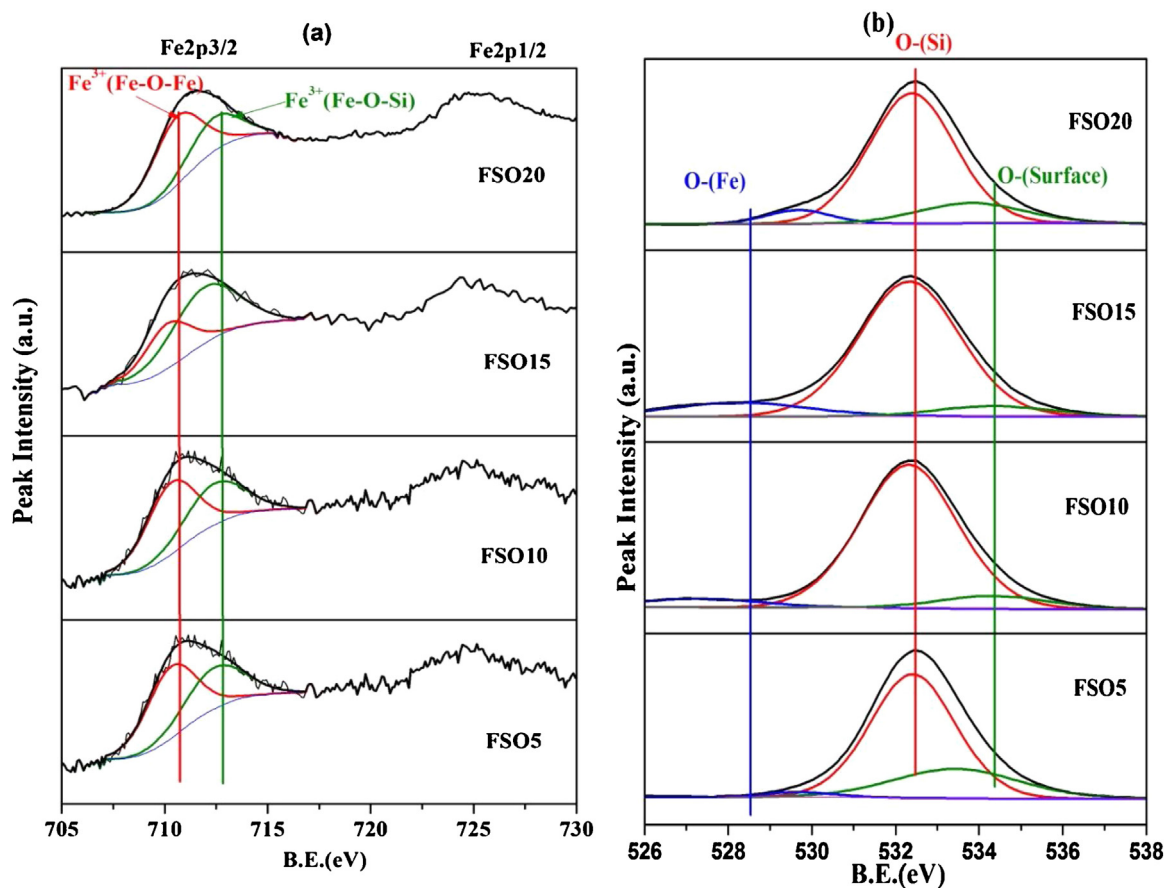


Fig. 4. X-ray photoelectron spectra of (a) Fe2p and (b) O1s of the $\text{Fe}_2\text{O}_3/\text{SiO}_2$ samples calcined at 1000°C .

Table 2

(a) The isomer shift (δ), quadrupole splitting (Δ), linewidth (Γ) of Fe^{3+} ions for $\text{Fe}_2\text{O}_3(x \text{ wt.}\%)/\text{SiO}_2$ samples ($x = 5, 10, 15$, and $20 \text{ wt.}\%$ calcined at 500°C) derived from Mössbauer spectra, recorded at room temperature. For the paramagnetic doublet, the quadrupole splitting $\Delta E_Q = e^2qQ/4$ (separation between two resonance lines of doublet). (b) The hyperfine field values (H_{hf}), isomer shift (δ), quadrupole splitting (Δ), linewidth (Γ) of Fe^{3+} ions for $\text{Fe}_2\text{O}_3(x \text{ wt.}\%)/\text{SiO}_2$ samples ($x = 10, 15$ and $20 \text{ wt.}\%$ heated at 1000°C) derived from Mössbauer spectrum, recorded at room temperature. Fitting quality $\chi^2 \cong 1$. Quadrupole splitting for magnetic sextet $\Delta(M) = (\Delta_{12} - \Delta_{56})/4$.

(a)						
Composition (Wt% of Fe ₂ O ₃)	Iron Sites Doublet (Fe ³⁺) Spm	Line width (<i>Γ</i>) mm/s ±0.02	Isomer shift (<i>δ</i>) mm/s ±0.007	Quadrupole splitting (<i>ΔE_Q</i>) mm/s ±0.01	Fitting quality (<i>χ</i> ²)	
5	γ-Fe ₂ O ₃	0.689	0.353	0.929	1.00	
10	γ-Fe ₂ O ₃	0.699	0.368	1.073	0.92	
15	γ-Fe ₂ O ₃	0.662	0.353	1.063	0.87	
20	γ-Fe ₂ O ₃	0.694	0.343	1.080	0.89	
(b)						
Composition (Wt% of Fe ₂ O ₃)	Iron Sites Phase (Fe ³⁺)	Relative area (<i>R_A</i>) %	Line width (<i>Γ</i>) mm/s	Isomer shift (<i>δ</i>) mm/s	Quadrupole splitting (<i>Δ</i>) mm/s	Hyperfine field (<i>H_{hf}</i>) Tesla
10	Sextet A – α- Fe ₂ O ₃	14.81	0.42 ± 0.19	0.40 ± 0.02	−0.28 ± 0.04	51.37 ± 0.15
	Sextet B – ε- Fe ₂ O ₃	25.90	0.31 ± 0.07	0.32 ± 0.02	−0.21 ± 0.03	44.52 ± 0.15
	Sextet C – ε- Fe ₂ O ₃	21.50	0.46 ± 0.18	0.29 ± 0.03	−0.09 ± 0.07	39.30 ± 0.39
	Sextet D – ε- Fe ₂ O ₃	26.88	0.30 ± 0.001	0.33 ± 0.07	−0.19 ± 0.13	25.62 ± 0.54
	Doublet (γ-Fe ₂ O ₃)	10.91	0.57 ± 0.06	0.15 ± 0.02	0.57 ± 0.03	–
15	Sextet A – α- Fe ₂ O ₃	11.33	0.38 ± 0.2	0.33 ± 0.02	−0.28 ± 0.04	50.94 ± 0.13
	Sextet B – ε- Fe ₂ O ₃	21.18	0.30 ± 0.08	0.35 ± 0.015	−0.17 ± 0.03	44.72 ± 0.11
	Sextet C – ε- Fe ₂ O ₃	21.79	0.34 ± 0.11	0.38 ± 0.02	−0.09 ± 0.05	38.75 ± 0.247
	Sextet D – ε- Fe ₂ O ₃	29.42	0.310 ± 0.074	0.30 ± 0.06	−0.24 ± 0.13	25.50 ± 0.57
	Doublet (γ-Fe ₂ O ₃)	16.28	0.73 ± 0.07	0.20 ± 0.02	0.57 ± 0.03	–
20	Sextet A – α- Fe ₂ O ₃	16.7	0.45 ± 0.14	0.37 ± 0.01	−0.22 ± 0.03	51.59 ± 0.07
	Sextet B – ε- Fe ₂ O ₃	27.7	0.34 ± 0.05	0.36 ± 0.02	−0.22 ± 0.03	45.01 ± 0.07
	Sextet C – ε- Fe ₂ O ₃	25.3	0.41 ± 0.09	0.34 ± 0.02	−0.07 ± 0.04	39.58 ± 0.18
	Sextet D – ε- Fe ₂ O ₃	21.5	0.63 ± 0.26	0.19 ± 0.04	−0.15 ± 0.07	26.08 ± 0.26
	Doublet (γ-Fe ₂ O ₃)	8.8	0.80 ± 0.097	0.16 ± 0.03	0.60 ± 0.06	–

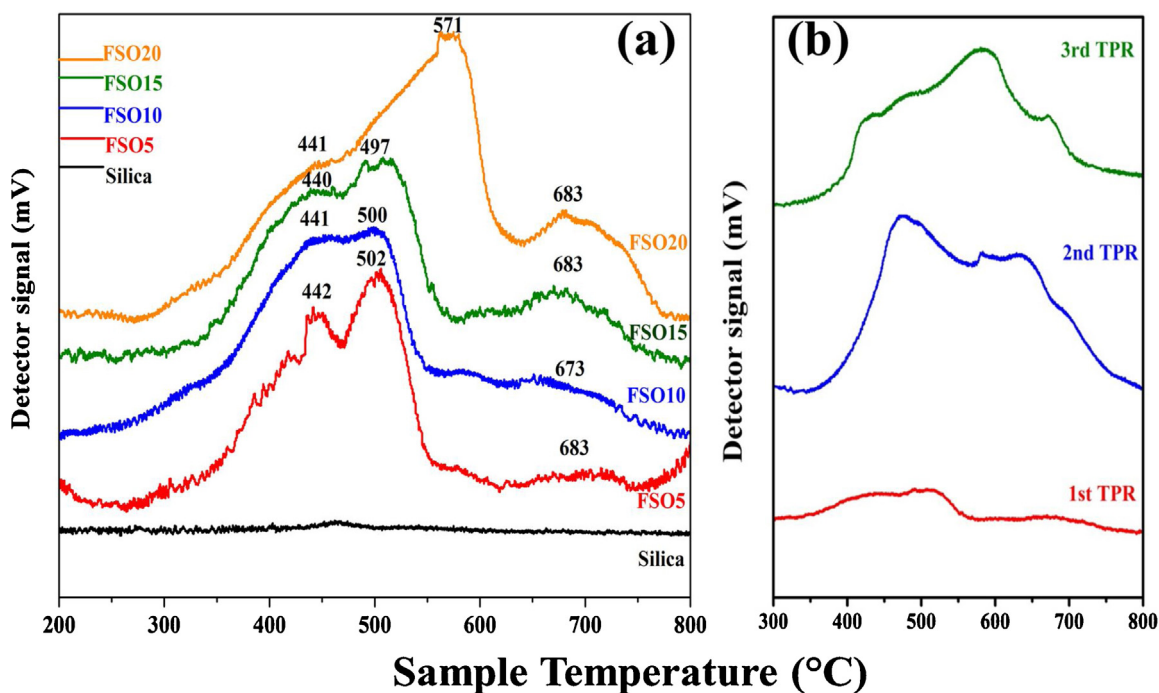


Fig. 5. (a) Temperature Programmed Reduction profiles of first cycle of the individual $\text{Fe}_2\text{O}_3/\text{SiO}_2$ samples calcined at 1000°C and (b) Successive TPR cycles for FSO15.

ate produced during the structural transformation of $\gamma\text{-Fe}_2\text{O}_3$ to $\alpha\text{-Fe}_2\text{O}_3$.

3.5. Surface features from X-ray photoelectron spectroscopy

The X-ray photoelectron spectra of the dispersed Fe_2O_3 samples calcined at 1000°C revealed crucial surface features. XPS is a surface sensitive technique in which the analytical volume is confined to approximately five monolayers [39]. Thus, the XPS spectra and its analysis provided information about surface or near surface elemental composition in our samples. The atom percent of each element as determined from the survey scan of our samples using Casa XPS package are listed in Table S1, (Supplementary Material). The Fe content was found to be much lower ($\sim 10\%$ of the desired value with respect to bulk composition) than expected for the three samples FSO5, FSO10 and FSO15. This clearly confirms our previous finding from N_2 adsorption desorption isotherms that the majority of Fe_2O_3 nanoparticles are immobilized within the porous network of SiO_2 [40–42]. On the contrary, the surface Fe content in FSO20 sample was found to abruptly increase to more than 30% of the expected value indicating that with higher concentrations of Fe_2O_3 , the phenomenon of nanoparticle restriction within support pores, as observed for lower concentrations are reduced. Above a certain concentration of Fe, the Fe_2O_3 phase gets deposited outside the SiO_2 mesoporous structure. Thus, 15 wt.% Fe_2O_3 may be regarded as the optimum loading in SiO_2 to obtain dispersed $\text{Fe}_2\text{O}_3/\text{SiO}_2$ composition with maximum Fe_2O_3 confined within pores. The $\text{Fe}2p$ spectra of the four samples are shown in Fig. 4(a). For all the samples the $\text{Fe}2p_{3/2}$ peak appears at a binding energy of ~ 711 eV with a separation of ~ 13.6 eV from the $\text{Fe}2p_{1/2}$ peak characteristic of Fe^{3+} [25,42]. Whatever little Fe was detected could be fitted into two peaks – one at ~ 710.6 eV due to Fe^{3+} present in Fe–O–Fe linkages while another at a higher BE value of ~ 712.8 eV can be attributed to Fe^{3+} bound to the SiO_2 support i.e. in Fe–O–Si linkages. Interesting pattern was observed in the case for O1s spectra shown in Fig. 4(b). The O1s peak could be deconvoluted into three peaks – the main peak having a BE value of ~ 532.5 eV in all the samples attributed to O^{2-} present in the major oxide component i.e. SiO_2 matrix, a lower

intensity peak at the highest BE values between 533.5–534.5 eV assigned to chemisorbed surface oxygen or surface adsorbed water or hydroxyl moieties [43,44], while another minor peak appeared at much lower binding energy values (527 eV to 529 eV). This low intensity peak progressively increased in intensity as we moved from FSO5 to FSO20 indicating that the peak could be assigned to O^{2-} present in dispersed Fe_2O_3 . Further, this peak also displayed a shift in position from ~ 527 eV in case of lower Fe_2O_3 containing compositions viz. FSO5, FSO10 and FSO15 to ~ 529 eV for FSO20, which could probably be attributed again to decreased strain in Fe_2O_3 nanoparticles in FSO20 due to precipitation of phase outside the pores. The $\text{Si}2p$ X-ray photoelectron spectra of fresh samples calcined at 1000°C is shown in Fig.S8 (Supplementary Material) which confirms the presence of Si in $4+$ state.

3.6. Redox properties of the catalyst investigated by TPR/TPO

The redox properties of the $\text{Fe}_2\text{O}_3/\text{SiO}_2$ samples were investigated by recording the temperature programmed reduction (TPR)/oxidation (TPO) cycles. The first cycle TPR profile of all the samples calcined at 1000°C are plotted in Fig. 5(a). The support SiO_2 was found to be non-reducing (as seen in Fig. 5(a)) under the TPR experimental conditions. Thus, in the dispersed sample all the peaks correspond to the reduction of the dispersed Fe_2O_3 phase. An obvious feature in the TPR profiles was that the extent of reduction increased with an increase in Fe content i.e. the area under the curve which corresponds to the amount of hydrogen consumed increased [45], as we moved from FSO5 to FSO20. This signifies that the availability of catalyst Fe_2O_3 increases with increase in loading. All the samples show mainly three peaks – two lower temperature ($300\text{--}600^\circ\text{C}$) major peaks which were merged and a higher temperature ($650\text{--}750^\circ\text{C}$) minor peak. The peak maxima (i.e. the temperature at which maximum hydrogen was consumed) for the merged first and second peaks appeared at $\sim 430^\circ\text{C}$ and $\sim 500^\circ\text{C}$ respectively for the three lowest Fe_2O_3 content samples. The third peak or hump appeared at $\sim 680^\circ\text{C}$. Further, it can be noticed that the peak maxima for all the three peaks move to a considerable higher temperature for FSO20 which implies inferior reducibility

of FSO20 than other three. Since in FSO5, FSO10 and FSO15, Fe_2O_3 is mainly immobilized within the SiO_2 pores while in FSO20 in major amount outside the pore as a composite, the reducibility of the FSO20 sample is found to be weaker. Better immobilization in lower percentage (upto 15 wt.%) have stabilized the nanoparticles of Fe_2O_3 in SiO_2 and better reducibility (in terms of lower reduction temperature) is achieved. On the contrary, precipitation of considerable amount of Fe_2O_3 outside pores as a composite could not stabilize the nanoparticles and poorer reducible samples were obtained. Again, among the low weight percent dispersion having similar reduction profile, FSO15 possesses better reducing capabilities by virtue of highest Fe_2O_3 content and consequently largest area under the reducing peak.

It is reported that reduction of bulk Fe_2O_3 takes place successively in three steps, first due to Fe_2O_3 to Fe_3O_4 , then Fe_3O_4 to FeO and finally reduction of FeO to Fe with the ratio of the three reduction peak areas of 1:2:6 [25]. However, in our earlier study with bulk Fe_2O_3 two peaks were observed, a smaller peak at a lower temperature ($\sim 520^\circ\text{C}$) due to the first reduction step and a larger peak at higher temperature ($\sim 815^\circ\text{C}$) owing to the merging of second and third reduction steps [25]. The $\text{Fe}_2\text{O}_3/\text{SiO}_2$ samples in this study show significantly different reduction profiles. This, dissimilar behavior in reduction profiles of dispersed Fe_2O_3 as compared to bulk implies that different reduction mechanism exists. One suggestion given earlier by Gervasini *et al.* for $\text{Fe}_2\text{O}_3/\text{SiO}_2$ catalysts was that hydrogen reduces dispersed iron oxide to three different final products due to three reducing paths: (i) Fe^{3+} to Fe^{2+} (with fayalite- Fe_2SiO_4 formation), (ii) Fe_2O_3 to FeO and (iii) Fe_2O_3 to Fe [29]. Thus, complete reduction of Fe_2O_3 is inhibited due to the adherence of Fe_2O_3 with SiO_2 matrix or more specifically SiO_2 - Fe_2O_3 interactions i.e. presence of Fe-O-Si linkages as observed in XPS. To further investigate this aspect, successive three TPR cycles were carried out for all the samples with an oxidation step in between two successive TPR cycles. The first reduction cycle is found to be much meager than the second cycle, probably due to the effect of adhered silica matrix which hinders the complete reduction of iron oxide. The three successive cycles for FSO15 samples are shown in Fig. 5(b) (for other samples it is shown in Fig. S9, Supplementary Material). It is evident that the intensity of the reduction band increases in the second cycle for every sample and then remains almost constant. Since the amount of reducible Fe_2O_3 is constant for a particular sample in all cycles, this behavior observed in multi cycling cannot be interpreted unless we consider the strong Fe_2O_3 - SiO_2 interactions. In the first cycle silica acts as inhibitor for the reduction, and a sluggish reduction profile of Fe^{3+} to Fe^0 is observed i.e. Fe_2O_3 is partly reduced to Fe , FeO and also Fe_2SiO_4 . But in subsequent cycles (interspersed with TPO), the Fe_2O_3 phase gets segregated out and a lesser inhibited (or enhanced) reduction of Fe_2O_3 was observed. Evidently, TPR also supports the presence of strong support-active phase interactions or Fe-O-Si linkages as interpreted in the XPS observations. These Fe-O-Si linkages will be instrumental for stabilizing the Fe_2O_3 nanoparticles over SiO_2 during catalytic operation.

3.7. Compositional superiority of 15 wt.% Fe_2O_3 on SiO_2

The structural and redox properties clearly indicate a better prospect of FSO15 sample as catalyst with respect to the other compositions. In this work the deposition of Fe_2O_3 phase was done in succession i.e. FSO5 was prepared first and on that sample further Fe_2O_3 was deposited to form the FSO10 and so on. A limit was probably reached for FSO15 in which case we noticed several advantageous properties. Firstly, the pore size for FSO15 was found to be maximum for the same base SiO_2 support among all the samples. A plausible cause for the increase in pore size of SiO_2 on Fe_2O_3 deposition was that, as progressive dispersion was attempted to increase Fe_2O_3 concentration in support SiO_2 , the deposition

prompted destabilization of the SiO_2 porous structure to certain extent to accommodate the increased amount of Fe_2O_3 particles within pores. This reached a maxima for the 15 wt.% dispersed sample beyond which the SiO_2 was unable to accommodate any further Fe_2O_3 within the pores and thus an increased amount of Fe_2O_3 deposited outside the pores and the sample formed a combination of $\text{Fe}_2\text{O}_3/\text{SiO}_2$ dispersed system and SiO_2 - Fe_2O_3 nano-composite. This plausible phenomenon was supported by our surface area, pore size distribution and XPS observations. Further, TPR studies clearly suggested better redox properties for FSO15 although FSO20 contained higher content of reducible species. So, for a dispersed catalyst system, there is always an optimum amount of the active component (Fe_2O_3) that could be properly dispersed on a porous support (SiO_2) which is neither too small nor too large.

3.8. Morphological features of the catalyst studied by transmission electron microscopy

The transmission electron microscopy images of the Fe_2O_3 (15 wt. %)/ SiO_2 sample calcined at 500°C and 1000°C are shown in Fig. 6. From Fig. 6(a) it is clearly evident that the support SiO_2 particles are spherical with particle size in the range of ~ 40 – 60 nm diameter. The small dots marked by arrows could be noticed in Fig. 6(a) which might be attributed to Fe_2O_3 . However, to visualize the shape and size of the Fe_2O_3 nanoparticles dispersed on SiO_2 , HRTEM images showing the presence of the particles in form of fringes were obtained (Fig. 6(b)). Crystalline nanoparticles, with varied shape, some spherical with 2–3 nm diameter, some oval with 2–5 nm size, some rectangular having size less than 5 nm length are found to be embedded on the surface of amorphous SiO_2 in the 500°C sample. Inset in Fig. 6(b) showed a magnified view of the region marked in image. The inset shows typical lattice spacing of 0.25 nm, corresponding to the (311) plane of γ - Fe_2O_3 . The same sample after calcination at 1000°C , yielded Fe_2O_3 nanorods dispersed on amorphous SiO_2 . From Fig. 6(c) presence of nanorods with typical width of 5 nm could be noticed. These nanorods adhered together to form crystalline rods of larger width of the order of 10 nm or 15 nm. The (111) plane of ϵ -phase is evident along the nanorods with lattice spacing of ~ 0.39 nm from the magnified view of the selected area in Fig. 6(d). Such a considerable modification in morphological properties of dispersed Fe_2O_3 particles is due to simultaneous agglomeration and phase transformation from γ to ϵ - Fe_2O_3 . These TEM results confirmed the phase evolution of Fe_2O_3 nanoparticles immobilized in SiO_2 as inferred from the results of the XRD and Mössbauer spectroscopic studies. Further, the size and shape of the Fe_2O_3 nanoparticles observed under TEM seems to be highly depended on its crystal phase. The phase of Fe_2O_3 again depends on the calcination temperature and nature of support (SiO_2 in our case). To the best of our knowledge, ϵ - Fe_2O_3 nanorods dispersed on SiO_2 is employed as catalyst for high temperature sulfuric acid decomposition reaction for the first time.

The above findings would be highly useful for the rational design of Fe_2O_3 based heterogeneous nanocatalysts, as catalytic properties are highly depended on not only the size but also shape of the nanocrystals [46]. In such kind of morphology driven nanocatalysis, the desired catalytic activity and selectivity can be realized by tuning the shape, that is, the exposed crystal facets, of a nanocrystal catalyst. By our current efforts we exhibit how the size, shape of Fe_2O_3 nanocrystallites depended on the produced crystal phase which again is depended on the temperature of calcination. This phenomenon can effectively lead us to pathways for the design of iron oxide shape selective catalysts which can promote catalyst conversions and might also be highly selective for particular reactions wherever applicable. Specifically metal oxide nanorods have been found to be highly active for various reactions over their coun-

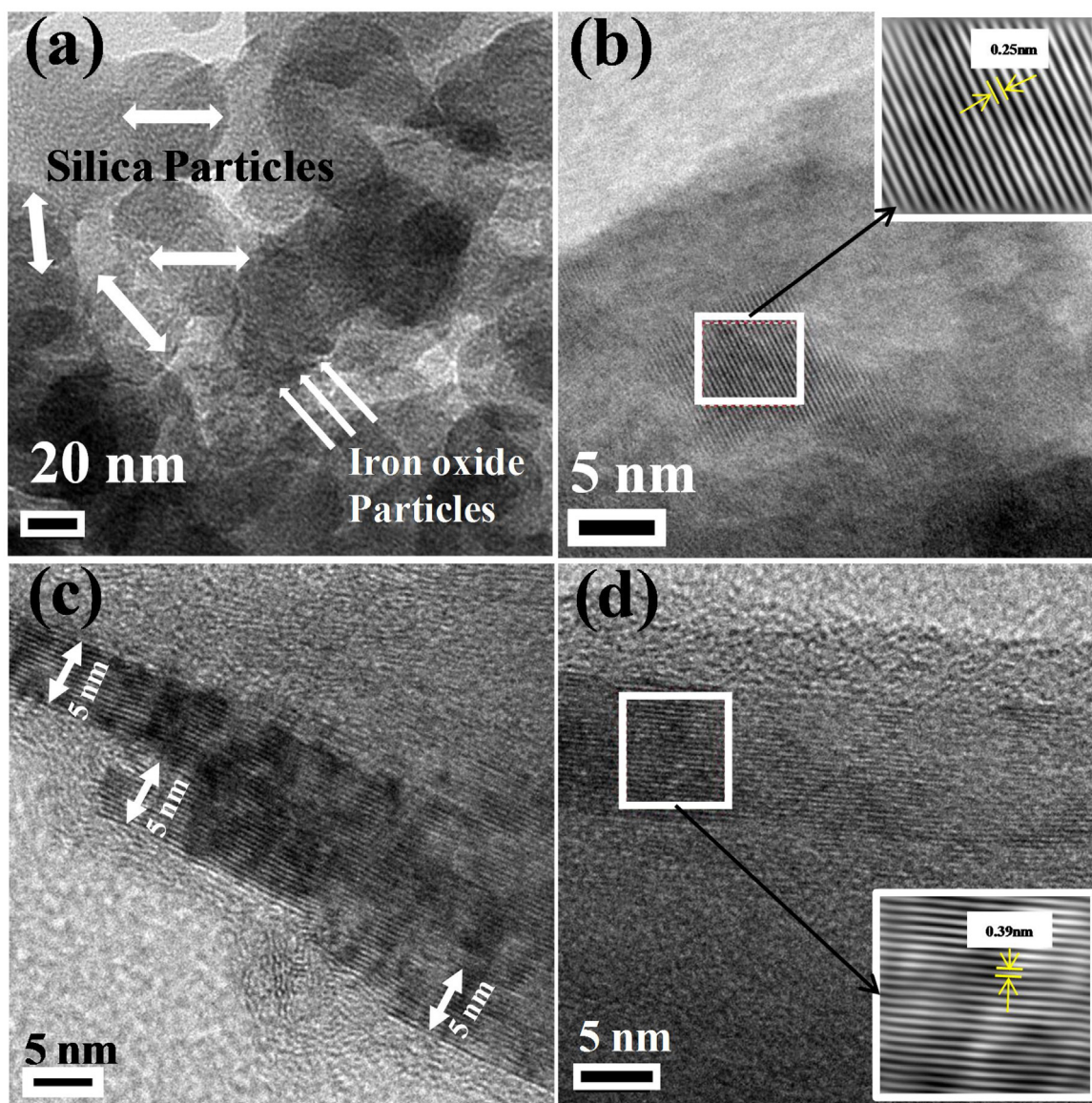


Fig. 6. (a) Low resolution (b) High Resolution TEM images of FSO15-500 fresh sample with magnified image of the selected area (c) and (d) High Resolution TEM images of the FSO15 sample.

terparts having identical composition but dissimilar morphology [46–48]. In our reaction the primary aim is not selectivity instead catalytic activity and stability which we will investigate by determining the high temperature catalytic properties.

3.9. Catalyst performance

The catalytic activities in the temperature range of 700–900 °C at a WHSV of 27 g acid g⁻¹ catalyst h⁻¹ of all the dispersed samples of 45–80 mesh were evaluated and are shown in Fig. 7(a). The SO₂ yield increased with an increase in temperature for all the samples which is due to kinetic factors [25]. Throughout the entire temperature range it is observed that the catalytic activity increases from FSO5 to FSO10 due to an increase in Fe content, then a significant increase for FSO15 and finally a drop in SO₂ yield for the extreme sample FSO20. FSO15 exhibited the highest activity throughout the entire temperature range. A maximum SO₂ yield of 92% at 900 °C was achieved over the FSO15 sample. As we move from FSO5 to FSO20, the Fe₂O₃ content gradually increases and accordingly FSO20 is expected to exhibit the highest

catalytic activity. But, earlier we established that 15 wt.% dispersion was the optimum Fe₂O₃ content to achieve maximum confinement within pores, optimum dispersion and best reducibility and hence it showed maximum catalytic activity. The FSO20 sample on the other hand suffered from deposition outside pores and consequently poorer reducibility. FSO5 and FSO10 were also sufficiently active but the Fe₂O₃ content was not sufficient enough on the surface to convert maximum possible SO₃ molecules to the product according to thermodynamic predictions. Based on the above findings it can be established that FSO15 is the superior catalyst with optimum amount of Fe₂O₃ content. So, further investigations were carried out with this composition to verify its practical applicability as a high temperature thermally stable catalyst viz. checking pore diffusion limitations with larger sized catalyst particles, long term catalytic property evaluation, evaluation of structural and morphological stability after long term operation.

Under practical conditions in an enhanced scale [25] the catalyst to be used is in a macro particulate form. In the above tests the catalyst used was in powder form (80–45 mesh). For larger sized particles the diffusion of the gaseous reactants (and prod-

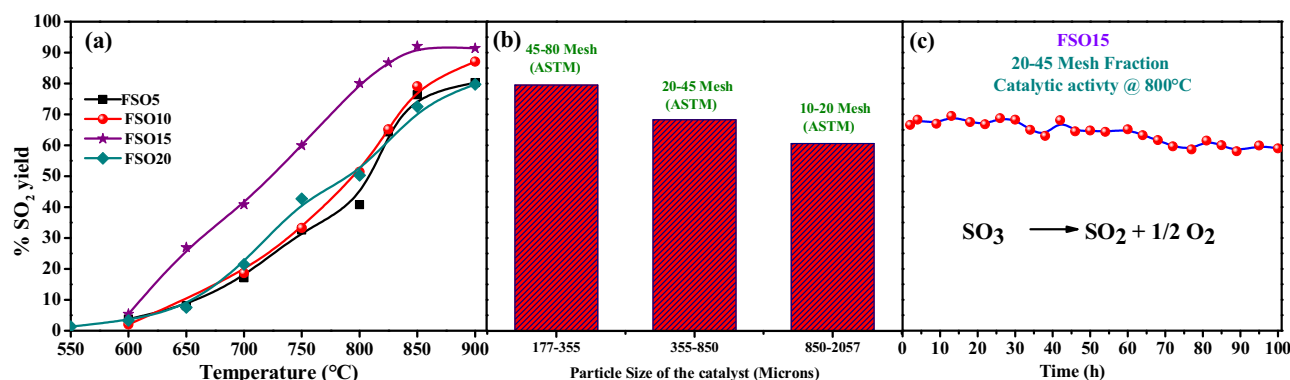


Fig. 7. (a) Temperature dependent activity profiles as a function of temperature of all the samples calcined at 1000 °C (b) The SO₂ yield as a function of mesh fraction of the FSO15 sample (c) catalytic activity of FSO15 (20–45 mesh) sample used in sulfuric acid decomposition reaction for 100 h time on stream at 800 °C. In all cases a WHSV of 27 g acid g⁻¹ catalyst h⁻¹ was maintained.

ucts) through the pores of the catalyst to reach (or go away from) an active site easily become rate limiting. To get a quantitative measure of this diffusion limitation, the SO₂ yield was evaluated at 800 °C for three different catalyst particle sizes 45–80 mesh, 20–45 mesh and finally 10–20 mesh. The result obtained is plotted in Fig. 7(b). It is evident that the SO₂ yield decreases from ~79% for the smallest particle fraction to ~60% for the largest fraction of the catalyst. As the mesh fraction of the catalyst decreases i.e. the particulate size increases, SO₂ yield decreases. This data gives us a quantitative estimate as to what extent the catalytic activity decreases as we employ bigger size granules.

Long term stability evaluation is mandatory before proposing a nanosized catalyst as a potential candidate for any high temperature reaction as it essentially determines its thermal stability under actual reaction conditions. We earlier found Pt/Al₂O₃ as thermally unstable in the long term catalytic evaluation due to agglomeration of Pt nanoparticles [11] and also Fe₂O₃ undergone sintering to a certain extent in 100 h under similar condition [25]. A 100 h time on stream performance for sulfuric acid decomposition was evaluated for FSO15 (20–45 mesh) and is plotted in Fig. 7(c). The catalyst shows sufficient stability with a decrease in SO₂ yield from ~70% to ~60% after 100 operations at a WHSV of 27 g acid g⁻¹ cat h⁻¹.

3.10. Ex-situ characterization of the 100 h spent catalyst

Post 100 h run the FSO15 catalyst was characterized ex-situ for changes in morphology, structure, oxidation state to investigate the mechanistic aspects. This would help us in identification of the catalytic properties that would play a key role in enhancing or decreasing rates. Further, ex-situ catalyst characterization post activity measurements would also enumerate the reasons that might have caused the catalytic activity decrease and hence would be able to convincingly indicate regarding catalyst stability and life.

3.10.1. Structural modifications on catalytic use

The powder XRD pattern of the fresh and spent FSO15 catalyst used for 100 h is shown in Fig. S10 (Supplementary Material). It is obvious that the small peaks due to various Fe₂O₃ phases present in the prepared catalyst are no longer visible in the powder XRD pattern of the spent catalyst and only the hump due to SiO₂ exist. Thus, whatever limited long range ordering was present in the prepared nanoparticles were probably lost on 100 h use. The amorphous nature of the support SiO₂ was still preserved.

The room temperature Mössbauer spectrum of the spent catalyst sample shows a single symmetric paramagnetic doublet as shown in Fig. S11 (Supplementary Material). In order to conclusively confirm the presence of any magnetic sextet due to ordering

Fe³⁺ ions we have recorded the Mössbauer spectrum at higher velocity scale (± 11.5 mm/s) but no such sextet was observed at room temperature in the Mössbauer spectrum. Thus the magnetic ordering present in the prepared sample was completely lost due to 100 h catalytic exploitation. Thus, the Mössbauer data supports our XRD findings. The values of Mössbauer parameters; isomer shift (δ), quadrupole splitting (ΔE_Q) and line width (Γ) are found to be 0.455 mm/s, 0.531 mm/s and 0.276 mm/s, respectively. These results gave us strong evidence regarding the nature of Fe species present in the spent sample. For amorphous iron (III) oxides, the values of δ and ΔE_Q are found to be in the range of $\delta \sim 0.33$ – 0.34 mm/s and $\Delta E_Q \sim 1.01$ – 1.11 mm/s [49,50] while the same for anhydrous iron (III) sulfate in the paramagnetic state at room temperature were found to be 0.49 mm/s and 0.29 mm/s, respectively relative to natural α -Fe foil [51]. Vaughan et al. observed $\delta = 0.39$ mm/s and $\Delta E_Q = 0.6$ mm/s for Fe₂(SO₄)₃ at atmospheric temperature and pressure [52]. Thus the Mössbauer study provides a strong indication that the Fe present in the sample is in the form of sulfate although its crystallinity might be poor.

3.10.2. Surface modifications on catalytic use from XPS studies

The XPS pattern of the spent catalyst was also reordered and analyzed. The surface elemental composition as determined from the XPS spectra is listed in Table S2 (Supplementary Material) for fresh FSO15 and used catalyst. An obvious outcome on 100 h use is the appearance of considerable amount of sulfur in addition to Si, O and Fe present in fresh catalyst (Table S2, Supplementary Material). The chemical nature of this sulfur was confirmed from the XPS spectra (Fig. 8a) where we see that the S2p peak appears at ~169 eV. This sulfate peak could be deconvoluted into three peaks, a major peak at ~169.4 eV due to ferric sulfate [25] another at ~168 eV due to Fe-sulfate attached with support SiO₂ i.e. the sulfated Fe in Fe-O-Si linkages and finally a minor peak at ~171.6 eV which is assigned to weakly adsorbed SO₂ on SiO₂ surface/pores [53,54]. The elemental Fe content which was ~11% of the theoretical content of Fe concentration in fresh catalyst reduced to ~8% in the spent catalyst, considering all the Fe₂O₃ being sulfated in the spent catalyst (Table S2 Supplementary Material). The most probable cause for this reduction in Fe content as compared to the fresh catalyst can be ascribed to formation to its surface sulfate species and thus Fe being masked. The Fe2p XPS pattern of the spent catalyst as compared with the fresh one is shown in Fig. 8b. The peak due to Fe2p appears to be quite broader than fresh catalyst and thus can be deconvoluted into four peaks – a low BE peak due to Fe²⁺, two due to Fe³⁺ in Fe₂O₃ (one Fe-O-Fe and other Fe-O-Si) and another at highest BE due to Fe³⁺ in its sulfate [25]. The O1s spectra of the fresh and spent catalyst shown in Fig. 8c shows that the major peak

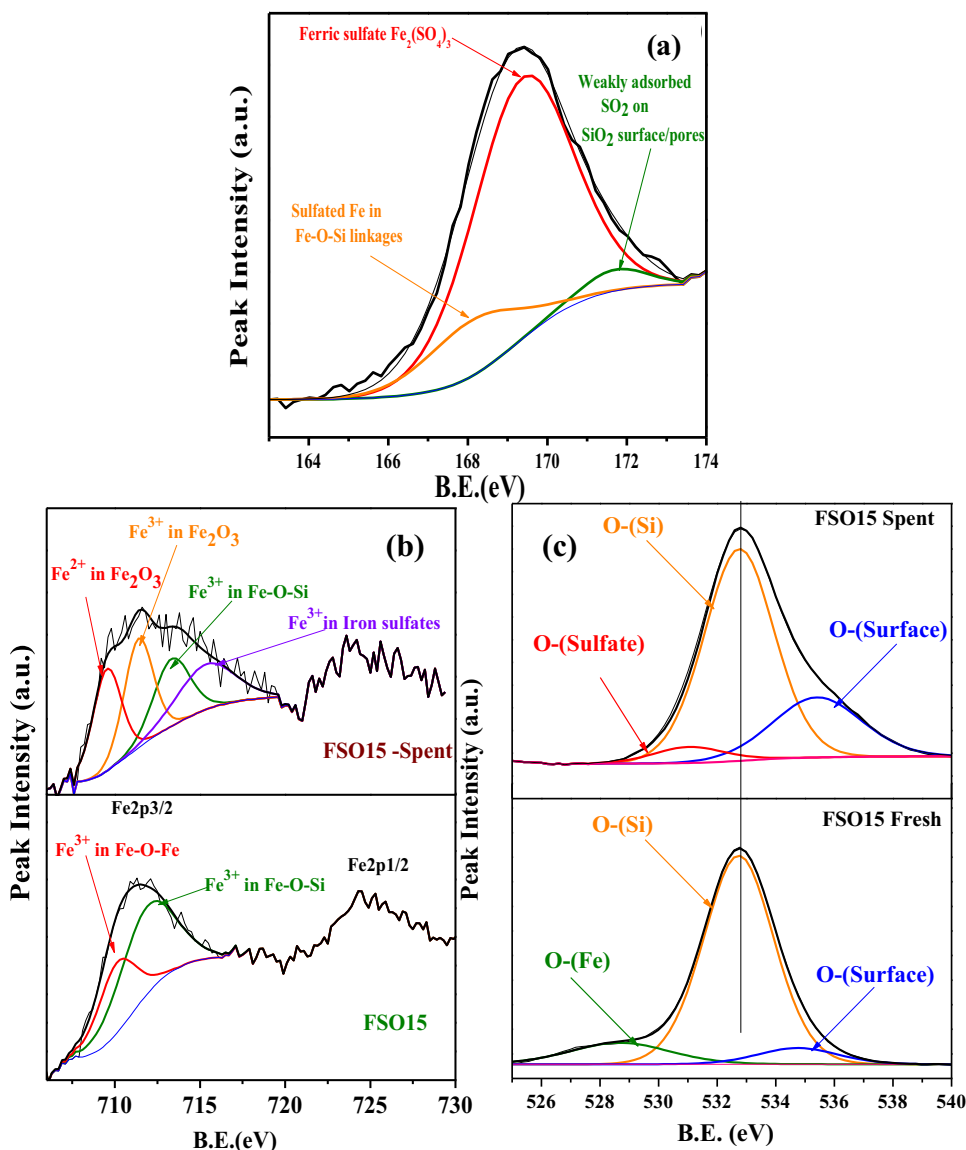


Fig. 8. (a) S2p X-ray photoelectron spectra of 100 h spent catalyst (b) Comparative Fe2p and (c) comparative O1s X-ray photoelectron spectra of fresh and spent catalyst after use for 100 h at 800 °C for sulfuric acid decomposition reaction.

due to O^{2-} in SiO_2 retains its position at ~ 532.5 eV, whereas a peak due to O^{2-} in Fe-sulfates appears at higher binding energy (531 eV) as compared to the O^{2-} in Fe_2O_3 in the fresh catalyst. The peak due to presence of chemisorbed oxygen/hydroxyl groups and adsorbed water is much broader in the spent catalyst.

3.11. Mechanistic aspects

The spent catalyst was also subjected to thermogravimetry-evolved gas analysis (TG-EGA) experiments, where the evolved gases from the sample when it was heated in a programmed mode were analyzed by a QMS. Fig. 9 shows the profile of the intensity of evolved gas, having mass number 64 (SO_2), in the temperature range of 250–900 °C. A small peak is observed at very low temperatures ~ 220 °C, which was never encountered in our earlier studies with ferrites [24] or iron oxides [25] or Pt/ Al_2O_3 [11]. This can be explained by the desorption of surface adsorbed or weakly adsorbed SO_2 species (observed in XPS) within the mesoporous network of SiO_2 . A sharp and a prominent peak appears at a peak maxima of ~ 645 °C which can be attributed to the decomposition of iron-sulfate species, since iron sulfate decomposes producing sul-

fur dioxide and metal oxide [25]. A very broad peak appeared at a further higher temperature with peak SO_2 evolution at ~ 850 °C. The nature of this temperature can be ascribed to the iron sulfates which are formed at the Fe_2O_3 - SiO_2 interface or at Fe-O-Si linkages and since these Fe-O species are attached to Si-O moieties the decomposition of the corresponding sulfate is considerable hindered. The evolution of SO_2 from the surface sulfate species corroborates our prior assumption [25] of concerted phenomenon of surface sulfate formation and decomposition as the most probable mechanism of the reaction. The proposed most probable mechanism is schematically shown in Fig. 10. Oxygen vacancies usually exist on the Fe_2O_3 nanoparticles at the high operating temperature by desorption of oxygen. This thermal oxygen evolution reaction requires proper functioning of the $\text{Fe}^{3+}/\text{Fe}^{2+}$ redox couple in $\text{Fe}_2\text{O}_3/\text{SiO}_2$ catalyst. The appearance of Fe^{2+} in the XPS of the spent catalyst supports the importance of the redox phenomenon of the Fe-species during catalytic use. Subsequent step is the formation of Fe-sulfate by chemisorption of SO_3 on these oxygen vacant sites and both the free Fe (Fe-O-Fe) and SiO_2 linked Fe (Fe-O-Fe) are sulfated [25]. This step is followed by the crucial sulfate decomposition yielding the product SO_2 and regenerating the metal oxide back.

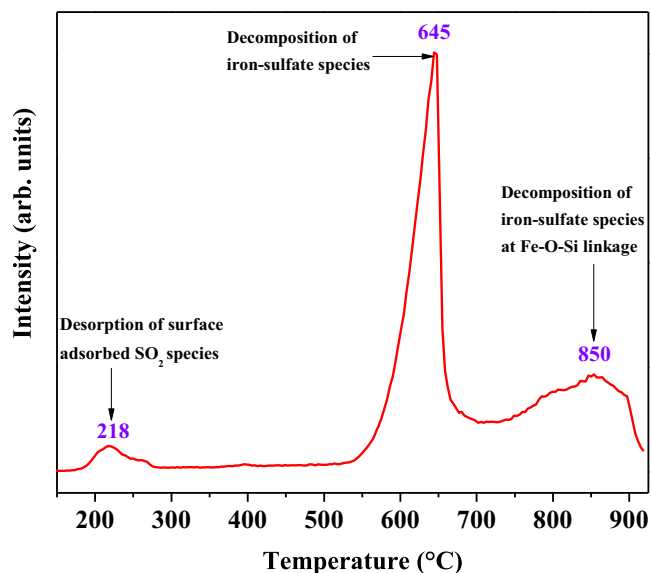


Fig. 9. Evolved gas analysis for mass number 64 as a function of temperature in mass spectrometer of the spent catalyst.

According to the TG-EGA results it is imperative that only the free Fe-sulfate decomposes at temperatures below 850 °C generating SO₂. The participation of the higher temperature decomposing sulfates or the mixed Fe-Si sulfates are probably meager instead their role is mostly to impart stability to the Fe₂O₃ nanoparticles. In our study the catalytic activity of the samples at 850 °C followed the order FSO15 > FSO10 > FSO5 > FSO20. As, the concentration of

active Fe₂O₃ species increases from FSO5 to FSO15 and the dispersion are retained the catalytic activity increases progressively. But, in FSO20 although there was an increase in Fe₂O₃ concentration the redox properties was found to be inferior and so was the catalytic activity. From the proposed most probable mechanism it is evident that facile sulfate decomposition and redox properties (i.e. easy working of Fe²⁺/Fe³⁺ couple) are crucial factors for determining reaction rates. In FSO20 the redox properties was found to be inferior as compared to other compositions. Thus, in case of Fe₂O₃/SiO₂ just by increasing the Fe₂O₃ content the redox and catalytic properties cannot be increased indefinitely, instead there exist an optimum concentration till which the dispersion will be proper yielding stable nanoparticles with superior redox and catalytic properties. Again, the nanoparticle stability is imparted in Fe₂O₃/SiO₂ by the Fe₂O₃-SiO₂ interactions i.e. the presence of Fe-O-Si linkages. To examine the extent of this stability the 100 h spent catalyst was also analyzed by transmission electron microscopy.

3.12. Morphological modifications on catalytic use

The low resolution TEM image of the spent sample indicates that the size and shape of SiO₂ particles are intact even after 100 h use at 800 °C. The HRTEM of the spent catalyst samples unambiguously exhibits the presence of amorphous spherical nanoparticles of ~8–10 nm size well distributed over the SiO₂ particles. As can be seen from the image (Fig. 11a) the crystalline nature of the ε-Fe₂O₃ as was observed in the fresh particles are completely lost which was further confirmed by the broad halo in the SAED pattern of the spent catalyst (Fig. 11b). The entire morphology gets modified i.e. the shape, size and crystallinity of the FSO15 sample was found to change on 100 h use. The shape of the particles is almost spheri-

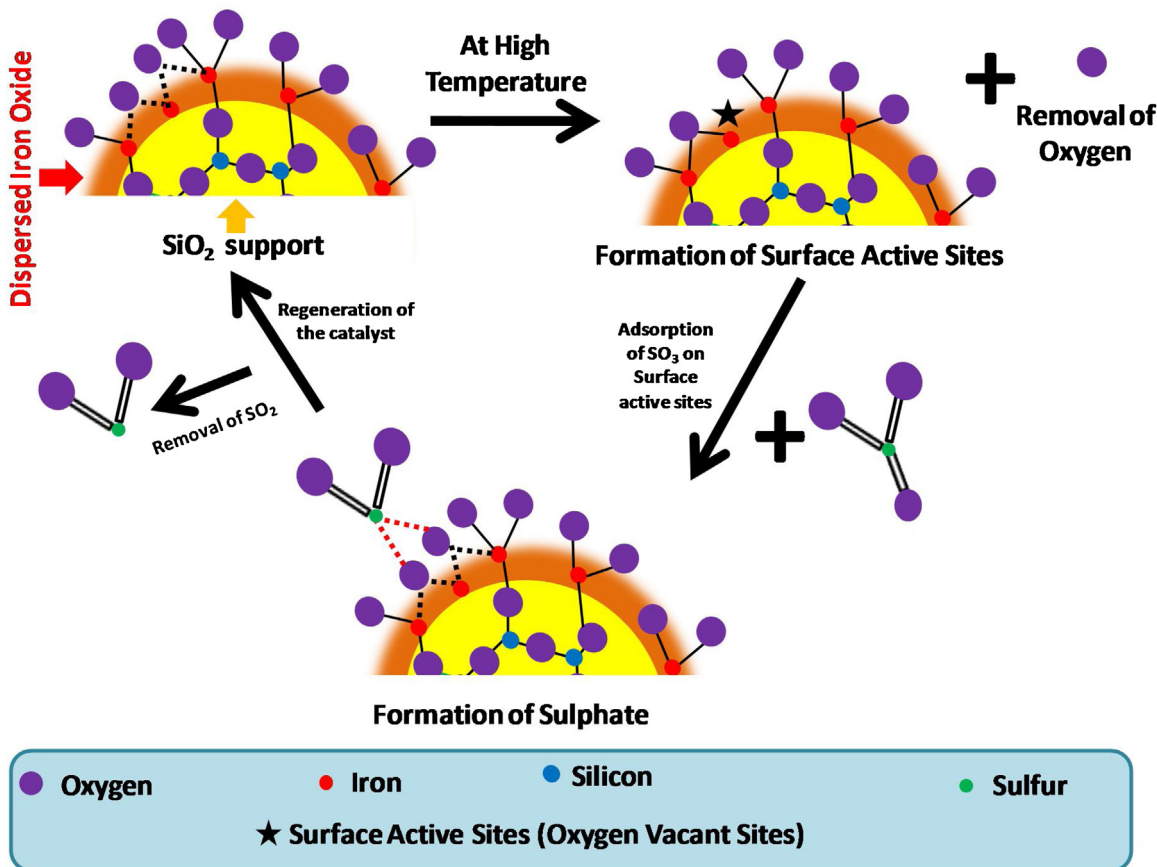


Fig. 10. Schematic representation of the most probable reaction mechanism proposed for sulfuric acid decomposition over silica supported iron oxide catalyst.

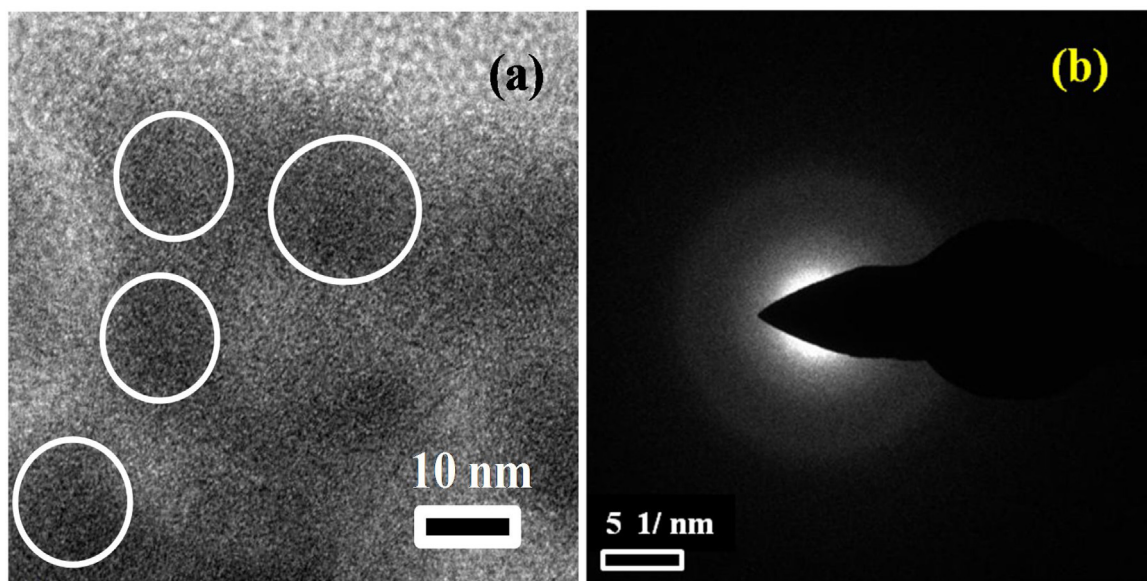


Fig. 11. (a) High Resolution TEM image and (b) SAED pattern of the of FSO15 sample used for 100 h at 800 °C for sulfuric acid decomposition reaction.

cal. The particle size of the amorphous Fe_2O_3 was of the order of ~ 10 nm as observed from the HRTEM images (Fig. 11). The particle size enhancement in this case is much smaller when compared to an average particle size increase to ~ 150 – 300 nm from ~ 100 nm in the case of Cr doped Fe_2O_3 used for sulfuric acid decomposition during 100 h operation at a much smaller WHSV of 3.4 g cat g^{-1} cat h^{-1} . This behavior suggests the reorganization of the active component on catalytic use, a phenomenon observed during several other catalysts on use in chemical processes [55,56]. The most probable cause for such a reorganization of the active component may be assigned to the nature of metal oxide-support interaction i.e. Fe_2O_3 - SiO_2 interaction and also the nature of reaction environment. Thus, schematically the morphological modifications during the entire course of preparation to catalytic use can be schematically described by Fig. S12 (Supplementary Material).

3.13. Role of Fe_2O_3 - SiO_2 interactions

In recent years it has emerged that enhanced stability and modified physico-chemical properties, even superior catalytic properties can be accomplished in the case of lattice matched support-active phase combinations [30,57,58] owing to electron density overlap of the support and dispersed phase. In some cases thermal stability for high temperature reactions has been attributed to core shell configurations viz. Pt@SiO_2 [59]. In our case of amorphous support and crystalline dispersed phase, we observe interestingly amorphisation and sulfation of dispersed phase. The structure of a heterogeneous catalyst is dynamic, as it adapts to the changes required depending upon the surrounding environment [59]. Thus, the surface morphology, structure and composition get significantly modified in order to adapt to our reaction environment. The sulfation of the Fe_2O_3 is obviously as a result of its involvement in SO_3 decomposition reaction. But, further to this, the participation (sulfation, desulfation and oxygen evolution) of Fe_2O_3 nanoparticles supported over amorphous SiO_2 in the decomposition reaction causes significant reorganization of the active phase Fe_2O_3 . The 15 wt.% Fe_2O_3 in SiO_2 yielded composition (FSO15) with superior redox property and catalytic activity but the Fe-O-Si linkages were not able to prevent the loss of crystallinity of the active phase and slight agglomeration of the Fe_2O_3 nanoparticles during rigorous catalytic use at 800 °C under harsh conditions of high

temperature, steam, SO_2 and SO_3 . But, they are able to stabilize the Fe_2O_3 nanoparticles to a considerable extent so that the catalyst retains significant catalytic activity even after 100 h of active operation at high temperature of 800 °C. These findings provide considerable impetus in the design and probable use of supported metal oxide nanoparticles as catalysts for high temperature reactions

4. Conclusions

Our study establishes that $\text{Fe}_2\text{O}_3/\text{SiO}_2$ is an active and stable catalyst for high temperature sulfuric acid decomposition reaction. The high activity can be ascribed to the nanoparticulate nature of the Fe_2O_3 phase while stability is imparted by the Fe-O-Si linkages i.e. the Fe_2O_3 - SiO_2 interactions. 15 wt percentage of Fe_2O_3 on the SiO_2 matrix was arrived as the optimum concentration of iron oxide exhibiting maximum pore confinement, superior redox properties and highest catalytic activity. Substantial structural and morphological rearrangements took place in the catalyst during 100 h use, but catalytic activity was retained to reasonable levels. A concerted phenomenon of surface sulfate formation and decomposition was found to be the most probable mechanism for decomposition of sulfuric acid over nanodispersed iron oxide catalyst. We believe that the present study will contribute to the design and probable use of supported nanoparticles for high temperature reactions. Further modifications in catalytic properties can be attempted by choosing exploiting more suitable supports to stabilize the active Fe_2O_3 phase or preparing compositions with stronger Fe-O-Si linkages or incorporating promoter elements viz. Cr, Cu etc.

Acknowledgements

The authors thank Shri. Siddhartha Kolay of Chemistry Division, BARC, for recording the TG-EGA runs, Dr. Rashmi Singh from RRCAT, Indore for recording the N_2 -BET adsorption desorption isotherms. AN gratefully acknowledges Department of Science and Technology (DST) New Delhi (No. DST/TSG/SH/2011/106) for the financial assistance from 2012 to 2014.

Appendix A. Supplementary data

Supplementary data associated with this article can be found, in the online version, at <http://dx.doi.org/10.1016/j.apcatb.2017.05.045>.

References

- [1] C.L. Muhich, B.W. Evanko, K.C. Weston, P. Lichty, X. Liang, J. Martinek, C.B. Musgrave, A.W. Weimer, *Science* 341 (2013) 540–542.
- [2] T. Kodama, N. Gokon, *Chem. Rev.* 107 (2007) 4048–4077.
- [3] W.C. Chueh, C. Falter, M. Abbott, D. Scipio, P. Furler, S.M. Haile, A. Steinfeld, *Science* 330 (2010) 1797–1801.
- [4] K. Onuki, S. Kubo, A. Terada, N. Sakaba, R. Hino, *Energy Environ. Sci.* 2 (2009) 491–497.
- [5] S. Yalcin, *Int. J. Hyd. Energy* 14 (8) (1989) 551–561.
- [6] L.C. Brown, J.F. Funk, S.K. Showalter, GA-A23373report, 2000.
- [7] V. Barbarossa, S. Brutti, M. Diamanti, S. Sau, G. De Maria, *Int. J. Hyd. Energy* 31 (2006) 883–890.
- [8] M. Machida, Y. Miyazaki, Y. Matsunaga, K. Ikeue, *Chem. Commun.* 47 (2011) 9591–9593.
- [9] D.M. Ginosar, L.M. Petkovic, A.W. Glenn, K.C. Burch, *Int. J. Hyd. Energy* 32 (2007) 482–488.
- [11] A.M. Banerjee, M.R. Pai, R. Tewari, N. Raje, A.K. Tripathi, S.R. Bharadwaj, D. Das, *Appl. Catal. B: Env.* 162 (2015) 327–337.
- [12] W.Z. Li, L. Kovarik, D. Mei, J. Liu, Y. Wang, C.H.F. Peden, *Nature Comm.* 4 (2013) 2481.
- [13] S. Lwin, I.E. Wachs, *ACS Catal.* 4 (2014) 2505–2520.
- [14] S. Royer, D. Duprez, F. Can, X. Courtois, C. Batiot-Dupeyrat, S. Laassiri, H. Alamdari, *Chem. Rev.* 114 (2014) 10292–10368.
- [15] T. Kim, G. Gong, B.G. Lee, K.Y. Lee, H.Y. Jeon, C.H. Shin, H. Kim, K.D. Jung, *Appl. Catal. A: Gen.* 305 (2006) 39–45.
- [16] D.M. Ginosar, H.W. Rollins, L.M. Petkovic, K.C. Burch, M.J. Rush, *Int. J. Hyd. Energy* 34 (2009) 4065–4073.
- [17] H. Abimanyu, K.D. Jung, K.W. Jun, J. Kim, K.S. Yoo, *Appl. Catal. A: Gen.* 343 (2008) 134–141.
- [18] G. Karagiannakis, C.C. Agrafiotis, C. Pagkoura, A.G. Konstandopoulos, D. Thomey, L.de Oliveira, M. Roeb, C. Sattler, *Int. J. Hyd. Energy* 37 (2012) 8190–8203.
- [19] G. Karagiannakis, C.C. Agrafiotis, A. Zygogianni, C. Pagkoura, A.G. Konstandopoulos, *Int. J. Hyd. Energy* 36 (2011) 2831–2844.
- [20] A. Giaconia, S. Sau, C. Felici, P. Tarquini, G. Karagiannakis, C. Pagkoura, C. Agrafiotis, A.G. Konstandopoulos, D. Thomey, L. de Oliveira, M. Roeb, C. Sattler, *Int. J. Hyd. Energy* 36 (2011) 6496–6509.
- [21] M. Machida, T. Kawada, S. Hebishima, S. Hinokuma, S. Takeshima, *Chem. Mater.* 24 (2012) 557–561.
- [22] T. Kawada, H. Yamashita, Q. Zheng, M. Machida, *Int. J. Hyd. Energy* 39 (2014) 20646–20651.
- [23] A.M. Banerjee, M.R. Pai, K. Bhattacharya, A.K. Tripathi, V.S. Kamble, S.R. Bharadwaj, S.K. Kulshreshtha, *Int. J. Hyd. Energy* 33 (2008) 319–326.
- [24] A.M. Banerjee, M.R. Pai, S.S. Meena, A.K. Tripathi, S.R. Bharadwaj, *Int. J. Hyd. Energy* 36 (2010) 4768–4780.
- [25] A.M. Banerjee, A.R. Shirole, M.R. Pai, A.K. Tripathi, S.R. Bharadwaj, D. Das, P.K. Sinha, *Appl. Catal. B: Env.* 127 (2012) 36–46.
- [26] A. Khan, P. Chen, P. Boolchand, P.G. Smirniotis, *J. Catal.* 253 (2008) 91–104.
- [27] J.A. Schwarz, C. Contescu, A. Contescu, *Chem. Rev.* 95 (1995) 477–510.
- [28] S. Bennici, A. Auroux, C. Guimon, A. Gervasini, *Chem. Mater.* 18 (2006) 3641–3650.
- [29] A. Gervasini, C. Messi, P. Carniti, A. Ponti, N. Ravasio, F. Zaccheria, *J. Catal.* 262 (2009) 224–234.
- [30] F. Jasim, I. Hamid, *Thermochim. Acta* 93 (1985) 65–68.
- [31] NIST webbook available online at: <http://webbook.nist.gov>.
- [32] S. Sakurai, A. Namai, K. Hashimoto, S. Ohkoshi, *J. Am. Chem. Soc.* 131 (2009) 18299–18303.
- [33] P. Brazda, J. Kohout, P. Bezduka, T. Kmjec, *Cryst. Growth Des.* 14 (2014) 1039–1046.
- [34] L. Machala, J. Tucek, R. Zboril, *Chem. Mater.* 23 (2011) 3255–3272.
- [35] J. Tucek, R. Zboril, A. Namai, S. Ohkoshi, *Chem. Mater.* 22 (2010) 6483–6505.
- [36] R. Zboril, M. Mashlan, D. Petridis, *Chem. Mater.* 14 (2002) 969–982.
- [37] R.M. Cornel, U. Schwertmann, *The Iron Oxides. Structure, Properties, Reactions and Uses*, Wiley, VCH, Weinheim, 1996.
- [38] T.P. Braga, A.N. Pinheiro, W.T. Herrer, Y.T. Xing, E. Baggio-Saitovitch, A. Valentini, *J. Mater. Sci.* 46 (2011) 766–773.
- [39] R. Kellner, J.-M. Mermet, M. Otto, M. Valcarcel, H.M. Widmer, *Surface and interface analysis*, in: J.M. Mermet, M. Otto, M. Valcarcel (Eds.), *Analytical Chemistry: A Modern Approach to Analytical Science*, Wiley-VCH Verlag GmbH and Co.KGaA, Weinheim, 2004, pp. 897–951 (chapter 27).
- [40] A.H. Lu, J.J. Nitz, M. Comotti, C. Weidenthaler, K. Schlichte, C.W. Lehmann, O. Terasaki, F. Schuth, *J. Am. Chem. Soc.* 132 (2010) 14152–14162.
- [41] Z. Wu, W. Li, P.A. Webley, D. Zhao, *Adv. Mater.* 24 (2012) 485–491.
- [42] C.D. Wagner, W.M. Riggs, L.E. Davis, J.F. Moulder, G.E. Muilenberg, *Handbook of X-Ray Photoelectron Spectroscopy*, Perkin-Elmer Corporation, Eden Prairie, MN, 1979.
- [43] J. Bao, X. Zhang, B. Fan, J. Zhang, M. Zhou, W. Yang, X. Hu, H. Wang, B. Pan, Y. Xie, *Angew. Chem. Int. Ed.* 54 (2015) 7399–7404.
- [44] S. Wang, W. Shi, Chao Lu, *Anal. Chem.* 88 (2016) 4987–4994.
- [45] A.M. Banerjee, M.R. Pai, Jagannath, S.R. Bharadwaj, *Thermochim. Acta* 516 (2011) 40–45.
- [46] K. Zhou, Y. Li, *Angew. Chem. Int. Ed.* 51 (2012) 602–613.
- [47] X. Xie, Y. Li, Z. Liu, M. Haruta, W. Shen, *Nature* 458 (2009) 746–749.
- [48] Y. Li, W. Shen, *Chem. Soc. Rev.* 43 (2014) 1543–1574.
- [49] N. Heiman, N. Kazama, *J. Appl. Phys.* 50 (1979) 7633.
- [50] C. Cannas, G. Concas, A. Falqui, A. Musinu, G. Spano, G. Piccaluga, *J. Non-Cryst. Solids* 286 (2001) 64–73.
- [51] L. Machala, R. Zboril, A. Gedanken, *J. Phys. Chem. B* 111 (2007) 4003–4018.
- [52] A.R. Champion, R.W. Vaughan, H.G. Drickamer, *J. Chem. Phys.* 47 (1967) 2583.
- [53] J.A. Rodriguez, T. Jirsak, S. Chaturvedi, M. Kuhn, *Surface Sci.* 442 (1999) 400–412.
- [54] J.A. Rodriguez, T. Jirsak, A. Freitag, J.Z. Larese, A. Maiti, *J. Phys. Chem. B* 104 (2000) 7439–7448.
- [55] N.J. Divins, I. Angurell, C. Escudero, V. Pérez-Dieste, J. Llorca, *Science* 346 (2014) 6209.
- [56] A. Locatelli, C. Sbraccia, S. Heun, S. Baroni, M. Kiskinova, *J. Am. Chem. Soc.* 127 (2005) 2351–2357.
- [57] X. Jin, L. Dang, J. Lohrman, B. Subramaniam, S. Ren, R.V. Chaudhari, *ACS Nano* 7 (2013) 1309–1316.
- [58] J. Treu, T. Stettner, M. Watzinger, S. Morkötter, M. Döblinger, S. Matich, K. Saller, M. Bichler, G. Abstreiter, J.J. Finley, J. Stangl, G. Koblmüller, *Nano Lett.* 15 (2015) 3533–3540.
- [59] S.H. Joo, J.Y. Park, Chia-Kuang Tsung, Y. Yamada, P. Yang, G.A. Somorjai, *Nat. Mat.* 8 (2009) 126–131.

Further reading

- [10] L.M. Petkovic, D.M. Ginosar, H.W. Rollins, K.C. Burch, P.J. Pinhero, H.H. Farrell, *Appl. Catal. A: Gen.* 338 (2008) 27–36.